
Hard exclusive photoproduction of photon-meson pairs: pseudoscalar channels π , η and η'

Nikola Crnković¹, Goran Duplancić¹, Saad Nabeebaccus², Kornelija Passek-K.¹
Bernard Pire³, Lech Szymanowski⁴, Samuel Wallon⁵,

¹*Division of Theoretical Physics, Ruđer Bošković Institute, HR-10002 Zagreb, Croatia*

²*Department of Physics and Astronomy, University of Manchester, Manchester M13 9PL, United Kingdom*

³*Centre de Physique Théorique, CNRS, École Polytechnique, I.P. Paris, 91128 Palaiseau, France*

⁴*National Centre for Nuclear Research, NCBJ, 02-093 Warsaw, Poland*

⁵*Université Paris-Saclay, CNRS, IJCLab, 91405 Orsay, France*

November 26, 2025

We investigate the hard exclusive photoproduction of photon-meson pairs at leading-twist and leading-order in perturbative QCD, and focus on pseudoscalar mesons $M \in \{\pi^\pm, \pi^0, \eta, \eta'\}$. Compact analytical expressions are obtained for the amplitudes involving quark generalized parton distributions, with the two-gluon components of the η and η' distribution amplitudes included. The numerical analysis is performed in the moderate- ξ region, where valence-quark GPDs are expected to be important. In this region, we find a strong impact of the pion-pole term in $\gamma\pi^\pm$ production, and a non-negligible effect for neutral mesons. We also observe a marked dependence of $\gamma\eta'$ photoproduction on two-gluon contributions. This process offers enhanced sensitivity to the shape of the GPDs already at leading-order, while the tested dependence on the meson distribution amplitude and the renormalization scale introduces further theoretical uncertainties, the latter emphasizing the need for next-to-leading-order corrections. Our results provide a concise analytical framework and a numerical baseline for future studies.

Contents

1	Introduction	2
2	Perturbative QCD framework for photon-meson photoproduction	4
2.1	Collinear kinematics of the hard-scattering subprocess	6
2.2	Factorization and amplitude decomposition	8
2.3	Nonperturbative inputs: DAs and GPDs	9
2.3.1	Meson distribution amplitudes	9
2.3.2	Generalized parton distributions	11
2.4	Analytical expressions for subprocess amplitudes	13
2.5	Compton-meson form factors in selected channels	16
3	Observables	19
3.1	Fully differential cross-section	19
3.2	Single differential and integrated cross-sections	20
4	Analysis of numerical results	21
4.1	GPD contributions and the role of the π pole.	23
4.2	Meson structure	25
4.3	Normalization and scale dependence	27
4.4	Numerical summary	28
5	Conclusions	28
A	Kinematics	30
B	Distribution amplitude formalism: convention and evolution	31
C	Hard-scattering amplitudes for mesons with non-symmetric DAs	33
D	Calculation of PV integrals	34
E	Compendium of numerical results	35
E.1	Fully differential cross-section	35
E.2	Single differential cross-section	40
E.3	Integrated cross-section	43

1 Introduction

In contrast to parton distribution functions (PDFs), generalized parton distributions (GPDs) probed in hard exclusive processes encode the multidimensional structure of the nucleon through three variables: the parton's average longitudinal momentum fraction x , the skewness ξ , and the momentum transfer t . They enter the process amplitudes through convolutions with the corresponding hard subprocess amplitudes. Consequently, extracting detailed information about GPDs, in particular their full dependence on the longitudinal momentum fraction x , remains a difficult task that requires combining input from several reactions. Most of the present knowledge comes from deeply virtual Compton scattering (DVCS) and deeply virtual meson production (DVMP), for which factorization has been rigorously

proven [1, 2, 3]. These reactions are supported by abundant experimental data, and their analyses have been carried out up to next-to-leading order (NLO) and beyond; for the phenomenological status see [4, 5, 6, 7] and references therein. These processes primarily access the chiral-even GPDs: parity-even (vector) H and E , and parity-odd (axial) \tilde{H} and \tilde{E} , while they lack sensitivity to the quark transversity GPDs at leading twist.

Photon-meson photoproduction, $\gamma N \rightarrow \gamma M N'$, has been proposed as a promising alternative to DVCS and DVMP, offering complementary access to GPDs [8, 9]. Similar to DVMP, this reaction probes quark flavors and includes gluon contributions already at leading order. An additional advantage is its sensitivity to transversity GPDs, which can be accessed at leading twist in the production of transversely polarized vector mesons.

Unlike DVCS ($\gamma^* N \rightarrow \gamma N$) and DVMP ($\gamma^* N \rightarrow M N'$), which are $2 \rightarrow 2$ processes involving essentially a single large scale, namely the incoming photon virtuality, photon-meson photoproduction is a $2 \rightarrow 3$ reaction that is characterized by two large scales and features more complex kinematics and a more elaborate leading-order (LO) hard-scattering amplitude. While the former processes provide mainly moment-type constraints, effectively probing GPDs at $x = \pm\xi$ at LO, the additional kinematic degrees of freedom in photon-meson photoproduction lead to a more detailed sensitivity to the x -dependence of GPDs [10]. A similar mechanism appears in double deeply virtual Compton scattering (DDVCS), where the presence of an additional scale also makes the process sensitive to $x \neq \pm\xi$ region already at LO [11].

Several other $2 \rightarrow 3$ processes have also been proposed. These include meson-meson photoproduction [12, 13, 14, 15], which provides access to transversity GPDs; two-photon photoproduction [16, 17, 18, 19], which has been studied at next-to-leading order (NLO); and the pion-nucleon to photon-photon process [20, 21], which represents the crossed counterpart of photon-meson photoproduction.

Photon-meson photoproduction has recently attracted considerable attention. The vector-meson channels, $\gamma\rho_L$ and $\gamma\rho_T$ [8], and the pseudoscalar channels, such as $\gamma\pi$ [9, 10], have been investigated at leading order. In particular, the sensitivity of $\gamma\pi$ photoproduction to the GPD structure has been explored in detail in [10], together with its crossed counterpart, $\pi N \rightarrow \gamma\gamma N'$ [21]. The feasibility of measuring these reactions at JLab, COMPASS, and EIC, as well as in ultraperipheral collisions at the LHC, has also been extensively studied [10, 22, 23]. Photoproduction of photon-heavy-meson pairs has likewise been analyzed [24], in which gluon contributions are leading and, due to the large meson mass, remain theoretically well behaved.

The factorization of photon-meson photoproduction has recently been established [25]. However, it was pointed out in [26, 27] that there are Glauber pinch singularities, contributing at the leading power, which spoil the factorisation in cases where two-gluon exchanges with the nucleon sector are allowed. There are potential remedies to save the phenomenology, e.g. in a modified factorisation framework [28, 29]. However, it is not the task of the present paper to address this. In this paper, we restrict ourselves to the contributions of quark GPDs at leading order, where there are no divergences appearing from the previously-mentioned factorisation breaking effects.

One of the motivations for the present work was the analysis of contributions involving the two-gluon DA. We show that, in contrast to the two-gluon exchange contributions associated with gluon GPDs, the two-gluon components of the η and η' distribution amplitudes do not lead to end-point or integration singularities. This is expected to be the case, since the Glauber pinch singularities that were identified in [26, 27] only affect cases where the Glauber exchange occurs between partons that connect incoming and outgoing asymptotic states. Therefore, the gluonic content of the η and η' mesons can be straightforwardly incorporated within the factorized framework for $\gamma N \rightarrow \gamma\eta(\eta')N'$, unlike the case of gluon GPDs in the nucleon sector discussed above.

In this work, we revisit the photoproduction of a photon-meson pair, $\gamma N \rightarrow \gamma M N'$, to systematize the results for pseudoscalar mesons $M \in \{\pi^\pm, \pi^0, \eta, \eta'\}$ and to include the two-gluon contributions to the η and η' channels. We obtain compact analytical expressions for the quark GPD contributions, which clarify the structure of the results and allow efficient numerical implementation.

Our phenomenological analysis is performed in the moderate- ξ kinematic region ($\xi > 0.1$). Only valence quarks were taken into account, and the effects of sea quarks and, in particular, gluons from the nucleon – relevant only in the neutral meson channels – are not considered. As discussed above, the latter would require a modified framework, and we leave the inclusion of these contributions for future work. Since valence quarks are significant in this ξ region, we believe that the valence-quark approximation in the neutral meson channel provides a consistent picture and useful insight into the contributions. In the case of charged pions, the sea-quark contributions cancel in the model used and gluons do not contribute. This kinematic region is of interest for the JLab and COMPASS/AMBER experiments in the near future. In this regime, the arguments for the dominance of the H and \tilde{H} GPDs based on the smallness of ξ [9, 22] are not applicable, and we therefore include the E and \tilde{E} GPDs in our analysis as well. Moreover, for moderate ξ , the pion-pole contributions can be significant, and we perform a dedicated study of the pion-pole contributions in all meson channels.

Furthermore, we discuss the meson structure in terms of DAs and its impact on γM photoproduction. The shape of pion DA, in addition to determining the internal structure of the produced pion, also affects the pion-pole contribution. For η and η' mesons, we analyze the role of the two-gluon components. The evolution of DAs and the dependence on the factorization scale are consistently taken into account, while the impact of the renormalization scale is examined and its implications for NLO calculations discussed. These aspects are investigated within the GPD model proposed in [30, 31, 32].

The aim of this work is to extend and systematize the analytical results, to investigate the individual contributing parts and the associated theoretical uncertainties within the kinematical range of interest, and to provide a reference numerical baseline for future experimental measurements, whose data would in turn enable a more precise determination of GPDs.

The paper is organized as follows. Section 2 presents the theoretical framework for evaluating photon-meson photoproduction amplitudes. We describe the collinear kinematics relevant for factorization and specify the perturbative and nonperturbative components, in particular the DAs and GPDs. Subsection 2.4 contains the main analytical results of this work, namely the compact analytical expressions for the subprocess amplitudes, including the two-gluon contributions to $\gamma\eta$ and $\gamma\eta'$ photoproduction. Section 3 summarizes the elements needed for the evaluation of observables used in the numerical analysis. Section 4 then presents a detailed discussion of the numerical results and their phenomenological implications. Section 5 concludes the paper with final remarks.

Additional material is provided in the Appendices. Appendices A and B give further details on kinematics and meson DAs and their evolution. Appendices C, D and E present selected technical and numerical results. In particular, Appendix C contains the general unsymmetrized form of the quark subprocess amplitudes, Appendix D explains the integration of the subprocess building blocks, and Appendix E gathers, for convenience, the figures illustrating the main numerical results.

2 Perturbative QCD framework for photon-meson photoproduction

In this work, we study the photoproduction of a photon-meson pair,

$$\gamma(q) + N(p_1) \rightarrow \gamma(k) + M(p_M) + N'(p_2), \quad (2.1)$$

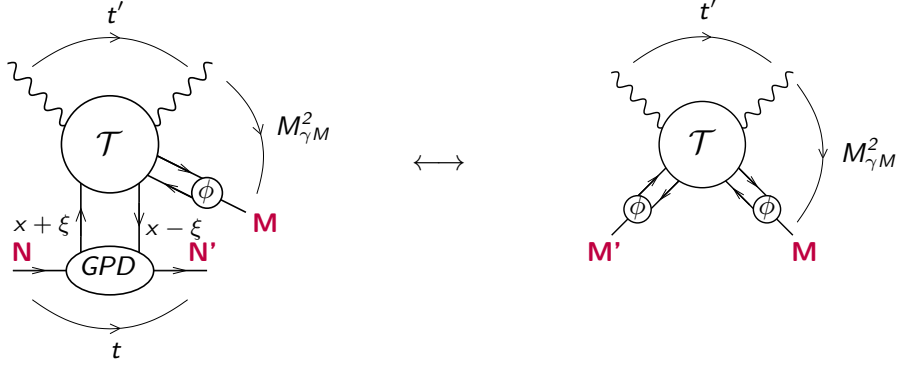


Figure 1: Left: Factorization of $\gamma N \rightarrow \gamma M N'$ process. Right: Brodsky–Lepage factorization for $\gamma M' \rightarrow \gamma M$ process.

where M denotes a pseudoscalar meson, $M \in \{\pi^\pm, \pi^0, \eta, \eta'\}$. The relevant scalar Lorentz invariants for this process include

$$\begin{aligned}
 S_{\gamma N} &= (q + p_1)^2, & t &= (p_2 - p_1)^2, & M_{MN'}^2 &= (p_M + p_2)^2, \\
 s' = M_{\gamma M}^2 &= (k + p_M)^2, & t' &= (q - k)^2, & u' &= (q - p_M)^2.
 \end{aligned}
 \tag{2.2}$$

Here, $S_{\gamma N}$ denotes the invariant mass of the incoming photon-nucleon pair, $t = (p_2 - p_1)^2$ is the squared momentum transfer between nucleons, $M_{MN'}^2$ represents the invariant mass of the outgoing meson-nucleon system, and $s' = M_{\gamma M}^2$ corresponds to the invariant mass of the outgoing γM pair. The variables s' , t' , and u' also serve as the Mandelstam variables of the partonic subprocesses $\gamma(q_1 \bar{q}_2) \rightarrow \gamma(q_1 \bar{q}_2)$ and $\gamma(q \bar{q}) \rightarrow \gamma(gg)$, which are discussed in more detail in the next subsection. One easily verifies that

$$s' + t' + u' = t + m_M^2. \tag{2.3}$$

The photoproduction of the (γM) pair, Eq. (2.1), is fully specified by the meson and nucleon masses, m_M and m_N , together with five independent Lorentz-invariant quantities¹. These can be taken either from Eq. (2.2) or expressed in terms of the dimensionless variables introduced in App. A. The factorization constraints further reduce the number of independent scalar quantities required. As explained below, we use four invariants: $s' = M_{\gamma M}^2$, u' , t , and $S_{\gamma N}$, or equivalent combinations of dimensionless variables.

The factorization of photon-meson photoproduction has been proved in Ref. [25], up to the subtleties regarding two-gluon exchanges with the nucleon sector mentioned in Sec. 1. Figure 1 illustrates the key ingredients of this factorization. When the momentum transfer to the outgoing nucleon, t , is small compared to the large invariant mass of the photon-meson pair, $M_{\gamma M}^2$, a kinematic configuration arises that closely resembles timelike Compton scattering (TCS) [33], where the final-state virtual photon with $Q^2 > 0$ is replaced by the γM system. The factorization conditions require a large momentum transfer t' , corresponding to large scattering angles, i.e., a large transverse momentum of the outgoing photon. It follows that the factorization of the $\gamma N \rightarrow \gamma M N'$ process in terms of nucleon GPDs is analogous to the large-angle Brodsky-Lepage factorization of the $\gamma M' \rightarrow \gamma M$ process, with the GPD corresponding to the meson M' distribution amplitude².

We refer to Refs. [8, 9, 22] and App. A for a detailed account of the general kinematics of the process

¹For fixed particle masses, a process with N external particles ($N \geq 4$) is characterized by $3N - 10$ independent Lorentz-invariant scalar products.

²This analogy parallels DVCS ($\gamma^* N \rightarrow \gamma N$) and the meson transition form factor ($\gamma^* \gamma \rightarrow M'$), as well as DVMP ($\gamma^* N \rightarrow M N'$) and the meson electromagnetic or meson-to-meson transition form factor ($\gamma^* M' \rightarrow M$).

$\gamma N \rightarrow \gamma M N'$. As usual, the momentum transfer between nucleons is defined as

$$\Delta^\mu = p_2^\mu - p_1^\mu, \quad (2.4)$$

$t = \Delta^2$, and the longitudinal momentum transfer (i.e., the skewness), is defined in terms of light-cone variables as

$$\xi = -\frac{\Delta^+}{P^+}, \quad \text{where} \quad P^\mu = p_1^\mu + p_2^\mu. \quad (2.5)$$

In what follows, we summarize the key ingredients required for the calculation of the subprocess amplitudes within the collinear approximation. For this purpose both the transverse momentum between nucleons, Δ_\perp , and the hadron masses are neglected, except for the nucleon mass retained in the skewness parameter

$$\xi = \frac{s'}{2(S_{\gamma N} - m_N^2) - s'}, \quad (2.6)$$

derived in Eq. (A.5).

2.1 Collinear kinematics of the hard-scattering subprocess

When the factorization conditions are satisfied, the amplitude for the process $\gamma N \rightarrow \gamma M N'$ can be represented as a convolution of the GPD, the meson DA, and the hard subprocess amplitude $\gamma q_1 \rightarrow \gamma q_2 (q_1 \bar{q}_2)$ or, equivalently,

$$\gamma (q_1 \bar{q}_2) \rightarrow \gamma (q_1 \bar{q}_2). \quad (2.7)$$

Effectively, we are considering the $\gamma(M') \rightarrow \gamma M$ process, where (M') denotes a partonic state carrying meson quantum numbers, but in our case described through GPDs. For neutral $C = +1$ states, the quark $(q\bar{q})$ Fock components can be replaced by gluon Fock states, gg . The contributions of gluon GPDs to the photoproduction of light neutral pseudoscalar mesons pose challenges due to Glauber pinch singularities, and the distinct cross-over behavior of gluon GPDs at $|x| = \xi$ compared to the end-point behavior of DAs [26, 27]. In this work, we calculate the quark GPD contributions, while the gg configurations are included solely in the outgoing meson. The corresponding subprocess amplitude then reads $\gamma q \rightarrow \gamma q (gg)$, i.e.,

$$\gamma (q\bar{q}) \rightarrow \gamma (gg). \quad (2.8)$$

The subprocess momenta are given by

$$q^\mu + (-\Delta)^\mu = k^\mu + p_M^\mu, \quad (2.9)$$

with

$$\begin{aligned} (-\Delta)^\mu &= y(-\Delta)^\mu + \bar{y}(-\Delta)^\mu, \\ p_M^\mu &= z p_M^\mu + \bar{z} p_M^\mu, \end{aligned} \quad (2.10)$$

decomposed in the collinear approximation in terms of the longitudinal momentum fractions z and y carried by the partons. Here we adopt the usual shorthand $\bar{v} = 1 - v$. While the meson momentum fractions satisfy $0 < z < 1$, the variable y , in the case of photoproduction of γM pair, serves as a

convenient parametrization defined by

$$y = \frac{\xi + x}{2\xi}, \quad \bar{y} = \frac{\xi - x}{2\xi}. \quad (2.11)$$

Here x denotes the usual ‘‘average’’ parton momentum fraction, $-1 < x < 1$, and consequently $(\xi - 1)/(2\xi) < y < (\xi + 1)/(2\xi)$.

In the collinear limit, where $t = \Delta^2 = 0$ and $p_M^2 = 0$, the subprocess Mandelstam variables introduced in (2.2), $s' = (q + (-\Delta))^2$, $t' = (p_M - (-\Delta))^2$, and $u' = (k - (-\Delta))^2$, satisfy

$$s' + t' + u' = 0. \quad (2.12)$$

The dimensionless variable α , introduced in App. A, takes the form

$$\alpha = \frac{-u'}{s'}, \quad \bar{\alpha} = \frac{-t'}{s'}, \quad (2.13)$$

and $0 < \alpha < 1$. The scattering angle θ of the outgoing photon in the center-of-mass frame of the subprocess in (2.7) or (2.8) (i.e. defined wrt to $q - \Delta$ system) can then be expressed through α as

$$\cos \theta = 2\alpha - 1. \quad (2.14)$$

Following (A.3), the subprocess momenta are given by

$$\begin{aligned} q^\mu &= n^\mu, & k^\mu &= \alpha n^\mu + \bar{\alpha} (2\xi) p^\mu + \kappa_\perp^\mu, \\ (-\Delta)^\mu &= 2\xi p^\mu, & p_M^\mu &= \bar{\alpha} n^\mu + \alpha (2\xi) p^\mu - \kappa_\perp^\mu, \end{aligned} \quad (2.15)$$

with the corresponding Sudakov decomposition in terms of the light-cone vectors p and n introduced in App. A. The momentum κ_\perp represents the relative transverse momentum between the outgoing photon and the meson, as defined in (A.3). According to (A.6), the invariant mass of the photon-meson pair and the relative transverse momentum are related by

$$-\kappa_\perp^2 = \alpha \bar{\alpha} s' = \frac{\sin^2 \theta}{4} s', \quad (2.16)$$

and both s' and the angle θ , or equivalently the transverse momentum κ_\perp , must be sufficiently large to ensure that the process lies in the hard-scattering regime.

Following Refs. [8, 9, 22, 23], in this work we adopt the axial gauge for photon polarizations,

$$\varepsilon_q \cdot p = \varepsilon_k \cdot p = 0. \quad (2.17)$$

The polarization vectors can then be written as

$$\begin{aligned} \varepsilon_q^\mu &= \varepsilon_{q_\perp}^\mu, \\ \varepsilon_k^\mu &= -\frac{\varepsilon_{k_\perp} \cdot k_\perp}{p \cdot k} p^\mu + \varepsilon_{k_\perp}^\mu. \end{aligned} \quad (2.18)$$

The $2 \rightarrow 2$ subprocess $\gamma(M') \rightarrow \gamma M$ is fully characterized by two scalar invariants, which we choose as s' and α . After accounting for the limit of small transverse momentum Δ_\perp , the full process

$\gamma N \rightarrow \gamma M N'$ is described by four invariants: s' , α , t , and $S_{\gamma N}$. The skewness ξ is defined as in (2.6).

2.2 Factorization and amplitude decomposition

The factorization of the $\gamma N \rightarrow \gamma M N'$ process proceeds similarly to DVCS and DVMP, with the amplitude being decomposed using Dirac spinor bilinears associated to the corresponding GPDs. In this work, we focus on the photoproduction of pseudoscalar mesons P , and considering allowed quantum numbers, two possible contributing configurations arise

$$\begin{aligned} \gamma(P) \rightarrow \gamma P : \quad \tilde{h}^+ &= \bar{u}(p_2) \gamma^+ \gamma^5 u(p_1) \rightarrow \tilde{H}, & \tilde{e}^+ &= \bar{u}(p_2) \frac{\Delta^+ \gamma^5}{2m_N} u(p_1) \rightarrow \tilde{E}, \\ \gamma(S) \rightarrow \gamma P : \quad h^+ &= \bar{u}(p_2) \gamma^+ u(p_1) \rightarrow H, & e^+ &= \bar{u}(p_2) \frac{i\sigma^{+\Delta}}{2m_N} u(p_1) \rightarrow E, \end{aligned} \quad (2.19)$$

where (P) and (S) denote states with pseudoscalar and scalar quantum numbers, respectively³. Specifically, the parity is $P = -1$ for P and $P = +1$ for S, while for neutral states the charge parity is $C = +1$. The total amplitude \mathcal{M} of the process can therefore be written as a sum

$$\mathcal{M} = \mathcal{M}^{\text{PP}} + \mathcal{M}^{\text{SP}} = \left(\tilde{\mathcal{H}} \frac{\tilde{h}^+}{P^+} + \tilde{\mathcal{E}} \frac{\tilde{e}^+}{P^+} \right) + \left(\mathcal{H} \frac{h^+}{P^+} + \mathcal{E} \frac{e^+}{P^+} \right), \quad (2.20)$$

where, by analogy with DVCS, we define the Compton-meson form factors (CMFFs) $\tilde{\mathcal{H}}$, $\tilde{\mathcal{E}}$, \mathcal{H} , and \mathcal{E} , named after the corresponding GPDs. These form factors factorize into a convolution of the relevant GPD, the meson DA, and the subprocess amplitude \mathcal{T} associated with subprocesses (2.7) and (2.8):

$$\begin{pmatrix} \tilde{\mathcal{H}}_{\text{M}} \\ \tilde{\mathcal{E}}_{\text{M}} \end{pmatrix} \sim \begin{pmatrix} \tilde{H}(x, \xi) \\ \tilde{E}(x, \xi) \end{pmatrix} \otimes^x \mathcal{T}_{\text{PP}}(x, \xi, z) \otimes^z \phi_{\text{M}}(z) = \begin{pmatrix} \tilde{H}(\xi(2y-1), \xi) \\ \tilde{E}(\xi(2y-1), \xi) \end{pmatrix} \otimes^y \mathcal{T}_{\text{PP}}(y, z) \otimes^z \phi_{\text{M}}(z), \quad (2.21)$$

$$\begin{pmatrix} \mathcal{H}_{\text{M}} \\ \mathcal{E}_{\text{M}} \end{pmatrix} \sim \begin{pmatrix} H(x, \xi) \\ E(x, \xi) \end{pmatrix} \otimes^x \mathcal{T}_{\text{SP}}(x, \xi, z) \otimes^z \phi_{\text{M}}(z) = \begin{pmatrix} H(\xi(2y-1), \xi) \\ E(\xi(2y-1), \xi) \end{pmatrix} \otimes^y \mathcal{T}_{\text{SP}}(y, z) \otimes^z \phi_{\text{M}}(z). \quad (2.22)$$

Here we introduce the notation

$$\otimes^x \equiv \int_{-1}^1 \frac{dx}{2\xi} = \int_{\frac{1}{2}(1-\frac{1}{\xi})}^{\frac{1}{2}(1+\frac{1}{\xi})} dy \equiv \otimes^y, \quad \otimes^z \equiv \int_0^1 dz, \quad (2.23)$$

where (2.11) has been taken into account.

We define the tensor amplitude $\mathcal{M}^{\mu\nu}$ through

$$\mathcal{M}(\lambda_q, \lambda_k) = \mathcal{M}_{\mu\nu} \varepsilon_q^\mu(\lambda_q) \varepsilon_k^{*\nu}(\lambda_k). \quad (2.24)$$

It is then convenient to introduce its general Lorentz decomposition, which, when applied to the subprocess amplitudes \mathcal{T} and with gauge invariance properly accounted for, facilitates the translation

³Besides providing compact notation, this convention clarifies the relation between the subprocess amplitudes and those obtained in the crossed process $\gamma\gamma \rightarrow M'M$ [34, 35, 36, 37, 38, 39].

between different photon gauges [9] and enables a direct comparison with established results in the literature, particularly for the crossed process $\gamma\gamma \rightarrow MM'$ [34, 35, 36, 37, 38, 39]. In this work, for the photon polarizations, we adopt the axial gauge (2.17), for which generally⁴

$$\begin{aligned}\mathcal{M}_{\text{ax}}^{\text{PP}} &= (\varepsilon_q \cdot \varepsilon_k^*) \mathcal{M}^{\text{PP}(0)} + (\varepsilon_q \cdot k) (q \cdot \varepsilon_k^*) \mathcal{M}^{\text{PP}(1)}, \\ \mathcal{M}_{\text{ax}}^{\text{SP}} &= (q \cdot \varepsilon_k^*) \varepsilon^{\varepsilon_q q(-\Delta)k} \mathcal{M}^{\text{SP}(1)} + (\varepsilon_q \cdot k) \varepsilon^{\varepsilon_k^* q(-\Delta)k} \mathcal{M}^{\text{SP}(2)}.\end{aligned}\quad (2.25)$$

Following Refs. [8, 9, 22, 23] and using (2.18), we express the Compton-meson form factors through the tensor decomposition

$$\begin{aligned}\tilde{\mathcal{H}} &= \tilde{\mathcal{H}}_A T_A + \tilde{\mathcal{H}}_B T_B, & \tilde{\mathcal{E}} &= \tilde{\mathcal{E}}_A T_A + \tilde{\mathcal{E}}_B T_B, \\ \mathcal{H} &= \mathcal{H}_{A5} T_{A5} + \mathcal{H}_{B5} T_{B5}, & \mathcal{E} &= \mathcal{E}_{A5} T_{A5} + \mathcal{E}_{B5} T_{B5},\end{aligned}\quad (2.26)$$

which employs the modified tensor structures⁵

$$\begin{aligned}T_A &\equiv \varepsilon_{q_\perp} \cdot \varepsilon_{k_\perp}^*, & T_B &\equiv (\varepsilon_{q_\perp} \cdot k_\perp) (k_\perp \cdot \varepsilon_{k_\perp}^*), \\ T_{A5} &\equiv (k_\perp \cdot \varepsilon_{k_\perp}^*) \varepsilon^{np\varepsilon_{q_\perp} k_\perp}, & T_{B5} &\equiv (k_\perp \cdot \varepsilon_{q_\perp}) \varepsilon^{np\varepsilon_{k_\perp}^* k_\perp}.\end{aligned}\quad (2.27)$$

2.3 Nonperturbative inputs: DAs and GPDs

2.3.1 Meson distribution amplitudes

At leading twist, pseudoscalar mesons can be represented by their $q_i \bar{q}_j$ Fock components, with the corresponding distribution amplitudes defined through hadronic matrix elements as

$$\langle M(p_M) | \bar{q}_i(-w) \mathcal{C}_M^{ij} \gamma^+ \gamma_5 q_j(w) | 0 \rangle = i p_M^+ f_M \int_0^1 dz e^{-i(z-\bar{z})p_M^+ w^-} \phi_M(z), \quad (2.28)$$

for a generic meson momentum p_M in the + light-cone direction. The matrix \mathcal{C}_M^{ij} encodes the flavour structure of the meson:

$$\begin{aligned}\pi^\pm : \quad u\bar{d}(d\bar{u}) &\quad \rightarrow \quad \mathcal{C}_{\pi^\pm} = \frac{1}{2} (\lambda_1 \mp \lambda_2), & \eta_8 : \quad \frac{1}{\sqrt{6}}(u\bar{u} + d\bar{d} - 2s\bar{s}) &\quad \rightarrow \quad \mathcal{C}_{\eta_8} = \frac{1}{\sqrt{2}} \lambda_8, \\ \pi^0 : \quad \frac{1}{\sqrt{2}}(u\bar{u} - d\bar{d}) &\quad \rightarrow \quad \mathcal{C}_{\pi^0} = \frac{1}{\sqrt{2}} \lambda_3, & \eta_1 : \quad \frac{1}{\sqrt{3}}(u\bar{u} + d\bar{d} + s\bar{s}) &\quad \rightarrow \quad \mathcal{C}_{\eta_1} = \frac{1}{\sqrt{n_f}} \mathbf{1}_f,\end{aligned}\quad (2.29)$$

with λ_i being the usual SU(3) Gell-Mann matrices, and $n_f = 3$. Additionally, the two-gluon (gg) Fock component contributes to the flavor-singlet pseudoscalar meson η_1 , whose gluon distribution amplitude is defined as

$$\langle \eta_1(p_M) | G^{+\nu}(-w) \tilde{G}_\nu^+(w) | 0 \rangle = \frac{(p_M^+)^2}{2\sqrt{n_f}} f_1 \int_0^1 dz e^{-i(z-\bar{z})p_M^+ w^-} \phi_{\eta_1 g}(z), \quad (2.30)$$

⁴The notation for the numbers in the round brackets are inspired from [9].

⁵Their relations to the four-vectors of the process are given by $T_A = \varepsilon_q \cdot \varepsilon_k^*$, $T_B = -\alpha (\varepsilon_q \cdot k) (\varepsilon_k^* \cdot q)$, $T_{A5} = \frac{-\alpha}{2\xi} \varepsilon^{\varepsilon_q q(-\Delta)k} (\varepsilon_k^* \cdot q)$, $T_{B5} = \frac{1}{2\xi} \varepsilon^{\varepsilon_k^* q(-\Delta)k} (\varepsilon_q \cdot k)$.

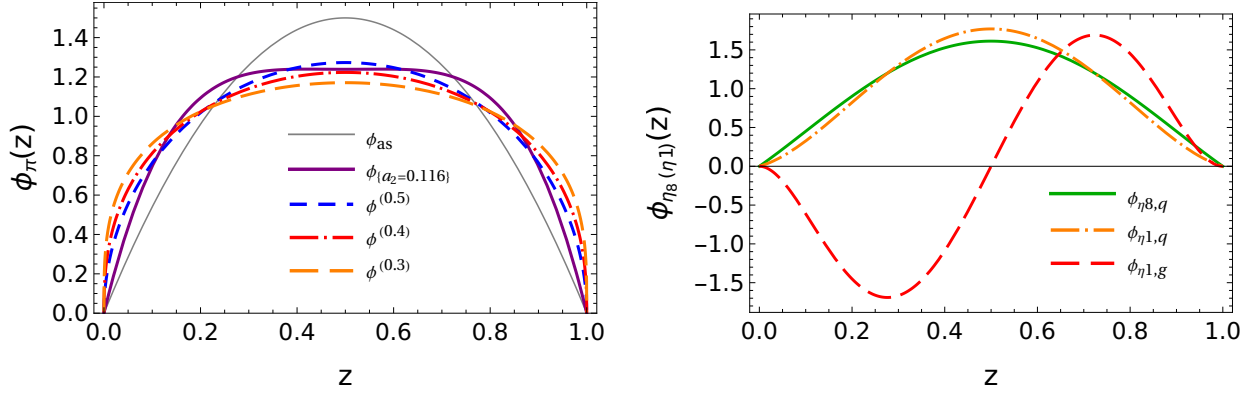


Figure 2: Left: Pion DAs. Shown are the asymptotic DA ($a_2 = 0$), the lattice-motivated DA with $a_2^\pi(\mu_0 = 2 \text{ GeV}) = 0.116$ [44] in the Gegenbauer representation (2.32), and the beta-function ansatz (2.35) for $\eta = 0.5, 0.4$, and 0.3 . Right: η_8 and η_1 DAs obtained from the Gegenbauer expansions (2.32) and (2.33), with coefficients evaluated at $\mu_0 = 2 \text{ GeV}$: $a_2^8 = -0.039$, $a_2^1 = -0.057$, and $a_2^g = 0.38$ [43].

where $\tilde{G}^{\mu\nu} = \frac{1}{2} \epsilon^{\mu\nu\gamma\delta} G_{\gamma\delta}$, with the convention that $\epsilon^{0123} = +1$. The quark and gluon distribution amplitudes, $\phi_{\eta_1 q} \equiv \phi_{\eta_1}$ and $\phi_{\eta_1 g}$, mix under evolution.

Due to pseudoscalar nature and isospin invariance, the pion⁶ and quark eta DAs are symmetric in ($z \rightarrow \bar{z}$), while two-gluon DAs are antisymmetric:

$$\phi_{\pi(\eta_8, \eta_1 q)}(z) = \phi_{\pi(\eta_8, \eta_1 q)}(\bar{z}), \quad \phi_{\eta_1 g}(z) = -\phi_{\eta_1 g}(\bar{z}). \quad (2.31)$$

The quark distribution amplitudes $\phi_{\pi(\eta_8, \eta_1 q)}$ are normalized to unity, while the flavor-singlet gluon DA, $\phi_{\eta_1 g}$, is, through QCD evolution, closely linked to its quark counterpart $\phi_{\eta_1 q}$. The convention for the gluon DA adopted here follows Refs. [40, 41, 42, 43].

It is often convenient to express the meson distribution amplitude as an expansion in the eigenfunctions of the LO evolution kernel—namely, the Gegenbauer polynomials $C_n^{3/2}(2z-1)$ and $C_n^{5/2}(2z-1)$ for the quark (2.28) and gluon (2.30) cases, respectively. The evolution of DA in this representation is available in a closed analytical form at both LO and NLO accuracy. Experimentally and on the lattice, however, only the first few expansion coefficients are accessible, with a_2 being the most reliably determined. Consequently, in this work we use the truncated expansions

$$\phi_M(z; \mu_F) = 6z(1-z) \left[1 + a_2^M(\mu_F) C_2^{3/2}(2z-1) \right], \quad (2.32)$$

$$\phi_{\eta_1 g}(z; \mu_F) = 30z^2(1-z)^2 a_2^g(\mu_F) C_1^{5/2}(2z-1). \quad (2.33)$$

The leading-order evolution is described in App. B.

For $M = \{\pi^+, \pi^-, \pi^0\}$ we compare two forms,

$$a_2^{\pi, \text{as}} = 0, \quad a_2^\pi(\mu_0 = 2 \text{ GeV}) = 0.116_{-17}^{+16}, \quad (2.34)$$

corresponding respectively to the asymptotic DA and the lattice moment-based result [44]. Recent studies suggest that the pion DA may in fact be broader, as indicated by momentum-fraction dependent lattice approaches that can, in principle, reconstruct the full DA shape [45, 46] and by various phenomenological analyses [47]. To explore this possibility, we also consider a symmetric beta-function

⁶As usual pion DA is taken the same for π^+ , π^- and π^0 .

ansatz,

$$\phi_{\pi}^{(\delta)}(z) = \frac{\Gamma(2+2\delta)}{\Gamma^2(1+\delta)} z^{\delta}(1-z)^{\delta}, \quad (2.35)$$

where the parameter δ controls the end-point behavior: smaller values correspond to broader DAs. We test several values- $\delta = 1/2$ (as in [48]), and the broader $\delta = 0.4$ and $\delta = 0.3$ suggested by the lattice results. The corresponding pion DAs are illustrated in Fig. 2.

For η and η' mesons, the octet state $M = \eta_8$ is described at leading twist by its $q\bar{q}$ component and quark DA (2.32), while the singlet $M = \eta_1$ also includes a gluon Fock state described by $\phi_{\eta_{1g}}$ (2.33). The two η_1 DAs, ϕ_{η_1} and $\phi_{\eta_{1g}}$, mix under QCD evolution. The definition of the gluon DA and the associated flavor-singlet evolution is convention dependent. In this work, we follow the convention of Ref. [42], outlined in App. B. The Gegenbauer coefficients are taken from the analysis of η and η' transition form factors in Ref. [41]

$$a_2^8 = -0.05 \pm 0.02, \quad a_2^1 = -0.12 \pm 0.01, \quad a_2^g = 0.63 \pm 0.17 \quad \text{at } \mu_0 = 1 \text{ GeV}. \quad (2.36)$$

The corresponding DAs, evolved to the scale $\mu = 2$ GeV, are depicted in Fig. 2.

The physical η and η' mesons are described in the octet-singlet basis as mixtures of η_8 and η_1 . This basis provides a natural framework for incorporating the two-gluon flavour-singlet components. Moreover, given the quality of the available data, the particle dependence and the mixing behaviour are incorporated solely through the decay constants. Within the two-angle mixing scheme, the decay constants are given by

$$\begin{aligned} f_{\eta}^8 &= f_8 \cos \theta_8, & f_{\eta}^1 &= -f_1 \sin \theta_1, \\ f_{\eta'}^8 &= f_8 \sin \theta_8, & f_{\eta'}^1 &= f_1 \cos \theta_1. \end{aligned} \quad (2.37)$$

The phenomenological values of these parameters, taken from Ref. [49], are

$$\begin{aligned} f_{\pi} &= 131 \text{ MeV}, & f_8 &= (1.26 \pm 0.06) f_{\pi}, & \theta_8 &= -(21.2 \pm 1.4)^{\circ}, \\ f_1 &= (1.17 \pm 0.04) f_{\pi}, & \theta_1 &= -(9.2 \pm 1.4)^{\circ}. \end{aligned} \quad (2.38)$$

The corresponding helicity amplitudes for η' and η production read

$$\begin{aligned} \mathcal{M}_{\eta} &= \cos \theta_8 \mathcal{M}_{\eta_8} - \sin \theta_1 \mathcal{M}_{\eta_1}, \\ \mathcal{M}_{\eta'} &= \sin \theta_8 \mathcal{M}_{\eta_8} + \cos \theta_1 \mathcal{M}_{\eta_1}, \quad \text{with } \mathcal{M}_{\eta_1} = \left(\mathcal{M}_{\eta_{1q}} + \mathcal{M}_{\eta_{1g}} \right). \end{aligned} \quad (2.39)$$

2.3.2 Generalized parton distributions

Similarly to the meson distribution amplitudes discussed in the preceding section, the leading-twist generalized parton distributions are conventionally defined through hadronic matrix elements in terms of Dirac spinor bilinears (2.19):

$$\langle p(p_2) | \bar{q}(-w) \gamma^+ \gamma_5 q(w) | p(p_1) \rangle = \int_{-1}^1 dx e^{-ixP^+w^-} \left(\tilde{h}^+ \tilde{H}^q(x, \xi, t) + \tilde{e}^+ \tilde{E}^q(x, \xi, t) \right), \quad (2.40)$$

$$\langle p(p_2) | \bar{q}(-w) \gamma^+ q(w) | p(p_1) \rangle = \int_{-1}^1 dx e^{-ixP^+w^-} \left(h^+ H^q(x, \xi, t) + e^+ E^q(x, \xi, t) \right), \quad (2.41)$$

which correspond to parity-odd (axial) and parity-even (vector) GPDs, respectively. The proton GPDs of quark flavour q are denoted as $\tilde{H}^q \equiv \tilde{H}_p^q$, with analogous notation for the remaining GPDs. Isospin symmetry relates proton and neutron distributions according to $\tilde{H}_p^u = \tilde{H}_n^d$, $\tilde{H}_p^d = \tilde{H}_n^u$, and $\tilde{H}_p^s = \tilde{H}_n^s$. In the case of $\gamma\pi^\pm$ photoproduction, transition GPDs contribute, and isospin relations lead to [50] $\tilde{H}_{pn}^{du} = \tilde{H}_{np}^{ud} = \tilde{H}_p^u - \tilde{H}_p^d$. Quark GPDs do not, in general, exhibit definite symmetry under the $(x \rightarrow -x)$ transformation. We therefore introduce the standard symmetric and antisymmetric combinations, which possess the required symmetry properties [50]

$$\tilde{H}^{q(\pm)}(x, \xi) \equiv \tilde{H}^q(x, \xi) \pm \tilde{H}^q(-x, \xi), \quad H^{q(\pm)}(x, \xi) \equiv H^q(x, \xi) \mp H^q(-x, \xi), \quad (2.42)$$

and analogously for \tilde{E} and E GPDs⁷.

In this work, we employ the GPDs proposed in [30, 31, 32] and summarized in [51], often referred to as the GK model. In this framework, the GPDs are constructed from their zero-skewness forms, whose products with suitable weight functions are interpreted as double distributions generating the skewness dependence of the GPDs [52]. For the adopted parameterization of the zero-skewness GPDs, together with the chosen weight function, the corresponding double-distribution integral can be evaluated analytically, and the Regge-inspired t -dependence added [31]. The parameterization of GPDs used in this work corresponds to initial scale $\mu_0 = 2$ GeV.

Additionally, we include the pion-pole contribution to \tilde{E} , following [51],

$$\tilde{E}_{\text{pole}}^u(x, \xi, t) = -\tilde{E}_{\text{pole}}^d(x, \xi, t) = \Theta(|x| \leq \xi) \frac{F_P(t)}{4\xi} \phi_\pi\left(\frac{x + \xi}{2\xi}\right), \quad (2.43)$$

where $F_P(t)$ represents the pseudoscalar form factor of the nucleon. Chiral symmetry constraints and low-energy theorems imply that the pole part of this form factor can be written as

$$F_P(t) = m_N f_\pi \frac{2\sqrt{2} g_{\pi NN} F_{\pi NN}(t)}{m_\pi^2 - t}. \quad (2.44)$$

Here, $g_{\pi NN} = 13.1$ denotes the pion-nucleon coupling constant, and $F_{\pi NN}(t)$ is the pion-nucleon vertex form factor, parameterized as

$$F_{\pi NN}(t) = \frac{\Lambda_N^2 - m_\pi^2}{\Lambda_N^2 - (t - t_0)}, \quad (2.45)$$

with $\Lambda_N = 0.44$ GeV and t_0 defined in (3.6). When the pion-pole term is included, the replacement $\tilde{E} \rightarrow \tilde{E} + \tilde{E}_{\text{pole}}$ (or equivalently, $\tilde{\mathcal{E}} \rightarrow \tilde{\mathcal{E}} + \tilde{\mathcal{E}}_{\text{pole}}$) is applied in our calculations.

The pion-pole contribution to \tilde{E} can be viewed as a specific example of a resonance-exchange contribution to GPDs. In particular, the pion exchange contributing to the region $-\xi \leq x \leq \xi$ of \tilde{E} may become significant at small t because of the proximity of the pion pole at $t = m_\pi^2$. This behavior is expected from chiral dynamics, where the pion is the lightest t -channel state and couples strongly through PCAC and the πNN interaction. The relative importance of the pion pole increases with ξ because it contributes only in the ERBL region $|x| \leq \xi$. As ξ grows, this region widens while the DGLAP domains shrink, so a larger fraction of the GPD is sensitive to t -channel exchange.

In the case of γM photoproduction, it corresponds to the right-hand diagram in Fig. 1 with $M' = \pi$, that is, to the amplitude of the subprocess $\gamma\pi \rightarrow \gamma M$. In DVCS, the pion pole contributes via the

⁷Note that the (\pm) superscript convention corresponds to the t -channel C -parity of the two partons. Multiplying it by the intrinsic parity, (-1) for parity-odd and $(+1)$ for parity-even GPDs, defines the signature σ , for which the quark GPDs satisfy $\text{GPD}(x) = -\sigma \text{GPD}(-x)$.

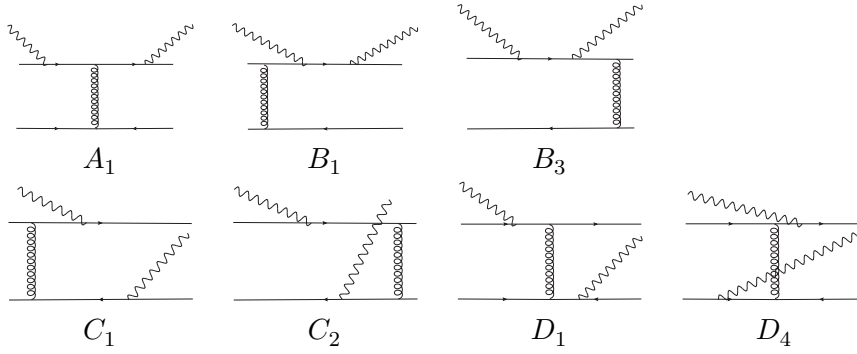


Figure 3: Representative Feynman diagrams contributing to $\gamma(q_1 \bar{q}_2) \rightarrow \gamma(q_1 \bar{q}_2)$ (2.7).

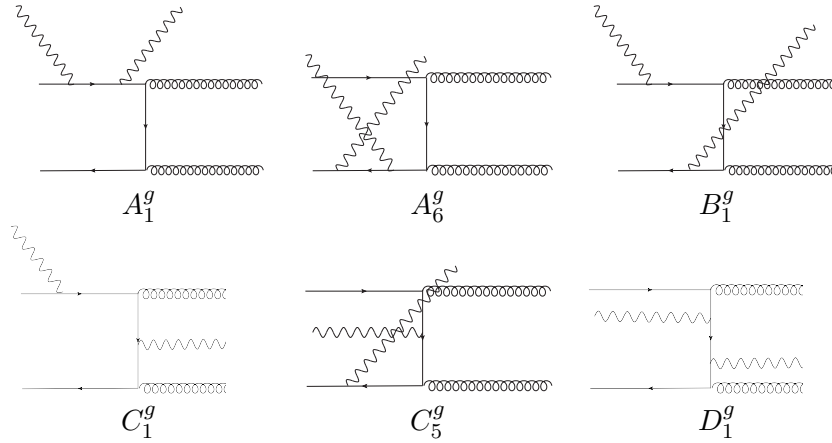


Figure 4: Representative Feynman diagrams contributing to $\gamma(q \bar{q}) \rightarrow \gamma(gg)$ (2.8).

transition form factor $\gamma^* \gamma \rightarrow \pi^0$, and may become important for some observables at moderate ξ [53]. In DVMP, the pion-pole term contributes for charged pions but vanishes for π^0 , and it has been found to be significant for $\xi > 0.1$ [54, 55, 32]. In that case, it corresponds to the pion electromagnetic form factor $\gamma^* \pi^\pm \rightarrow \pi^\pm$, and since perturbative QCD predictions lie below the experimental measurements, the phenomenological analyses for DVMP used the parametrization of the experimental data for the pion form factor [32]. In the present study, such an approach is not possible, as there are no data available for Compton scattering on a pion in the kinematical region of interest. The crossed process $\gamma\gamma \rightarrow M'M$ has also been measured, and there as well, the theoretical predictions lie below the data. Hence, our estimate of the pion-pole contribution based on the pion DA may underestimate its actual impact.

2.4 Analytical expressions for subprocess amplitudes

One of the main results of this work is the completion and systematization of the expressions for the subprocess amplitudes $\gamma(q_1 \bar{q}_2) \rightarrow \gamma(q_1 \bar{q}_2)$ (2.7) and $\gamma(q \bar{q}) \rightarrow \gamma(gg)$ (2.8). The latter are calculated here for the first time in the context of photon-light-meson photoproduction. Representative Feynman diagrams are shown in Figs. 3 and 4, while the contributions are evaluated using the projectors given in App. B.

The same diagrams also contribute to the t -channel subprocesses (as opposed to the above s -channel case), $\gamma\gamma \rightarrow (q_1 \bar{q}_2)(q_2 \bar{q}_1)$ and $\gamma\gamma \rightarrow (q \bar{q})(gg)$, and thus to the hadronic processes $\gamma\gamma \rightarrow MM'$ and $MN \rightarrow \gamma\gamma N'$. The former has been extensively studied in the past [34, 35, 36, 37, 38, 39], even at NLO [56], while the latter has more recently attracted interest in the framework of GPD-based descriptions [20, 21], being the crossed process of γM photoproduction. The general $2 \rightarrow 2$ subprocess amplitudes

$\gamma(q_1\bar{q}_2) \rightarrow \gamma(q_1\bar{q}_2)$ and $\gamma(q\bar{q}) \rightarrow \gamma(gg)$ are identical across these applications and can be, as in (2.24), expressed in terms of Mandelstam variables and photon polarization vectors. The specific choice of photon gauge, reference frame, and kinematical setup - in particular, the range of momentum fractions (whether linked to DAs or GPDs) and the definitions and signs of Mandelstam variables (for instance, $s' \leftrightarrow t'$ between s - and t -channel subprocesses) - differentiate these cases. To illustrate this point, although the same diagrams contribute, Compton scattering on a meson M ($\gamma M \rightarrow \gamma M$) contains cuts, i.e., imaginary parts, already at LO, whereas the crossed meson-pair photoproduction ($\gamma\gamma \rightarrow MM$) is real at LO. In the literature, the fully general forms of these amplitudes are not usually presented; however, as outlined in [9], using the general Lorentz decomposition of $\mathcal{T}_{\mu\nu}$ and imposing gauge invariance constraints, one can derive relations between the amplitudes in different gauges. We applied this method to compare our results with those for $\gamma\gamma \rightarrow MM'$ from the literature-particularly the gluon contributions from [36]-and found agreement up to $i\epsilon$ terms, which depend on kinematics.

Taking into account the decomposition introduced in Sec. 2.2, we express the amplitudes corresponding to the subprocess $\gamma(q_1\bar{q}_2) \rightarrow \gamma(q_1\bar{q}_2)$ in the following form:

$$\mathcal{T}_{\text{PP}}^{[ij]} = \left(e_i^2 \mathcal{T}_A^{(i)} + e_j^2 \mathcal{T}_A^{(j)} + e_i e_j \mathcal{T}_A^{(ij)} \right) T_A + \left(e_i^2 \mathcal{T}_B^{(i)} + e_j^2 \mathcal{T}_B^{(j)} + e_i e_j \mathcal{T}_B^{(ij)} \right) T_B, \quad (2.46)$$

and

$$\mathcal{T}_{\text{SP}}^{[ij]} = \left(e_i^2 \mathcal{T}_{A5}^{(i)} + e_j^2 \mathcal{T}_{A5}^{(j)} + e_i e_j \mathcal{T}_{A5}^{(ij)} \right) T_{A5} + \left(e_i^2 \mathcal{T}_{B5}^{(i)} + e_j^2 \mathcal{T}_{B5}^{(j)} + e_i e_j \mathcal{T}_{B5}^{(ij)} \right) T_{B5}, \quad (2.47)$$

where the definitions in (2.27) apply. A total of twenty diagrams contribute, with representative ones shown in Fig. 3: the A -type (4) and B -type (8) diagrams enter the e_i^2 - and e_j^2 -proportional terms, while the C -type (4) and D -type (4) diagrams contribute to the $e_i e_j$ -proportional terms. These can be grouped into four gauge-invariant sets related by symmetry relations:

$$\begin{aligned} \mathcal{T}_X^{(i)}(y, z) &= \mathcal{T}_X^{(j)}(\bar{y}, \bar{z}), & \mathcal{T}_X^{(ij)}(y, z) &= \mathcal{T}_X^{(ij)}(\bar{y}, \bar{z}), \\ \mathcal{T}_{X5}^{(i)}(y, z) &= -\mathcal{T}_{X5}^{(j)}(\bar{y}, \bar{z}), & \mathcal{T}_{X5}^{(ij)}(y, z) &= -\mathcal{T}_{X5}^{(ij)}(\bar{y}, \bar{z}), \end{aligned} \quad (2.48)$$

that is, they are symmetric under $(y, z) \rightarrow (\bar{y}, \bar{z})$ for PP contributions and antisymmetric for SP ones. The complete and systematized results, organized using the compact (y, z) notation and applicable to the photoproduction of any light pseudoscalar meson-including kaons described by non-symmetric DAs-are provided for completeness in Appendix C. Our concise analytical forms are consistent with previous work⁸ [9].

In this work we focus on pseudoscalar mesons whose quark distribution amplitudes are symmetric under $(z \rightarrow \bar{z})$ (2.31). Exploiting this property, and introducing the symmetric ($\tilde{H}^{q(+)}$, $\tilde{E}^{q(+)}$, $H^{q(-)}$, $E^{q(-)}$) and antisymmetric ($\tilde{H}^{q(-)}$, $\tilde{E}^{q(-)}$, $H^{q(+)}$, $E^{q(+)}$) GPD combinations (2.42), we can write the results in a compact analytical form. We recall that, according to the definition of the variable y (2.11), the $(x \rightarrow -x)$ symmetry corresponds to $(y \rightarrow \bar{y})$. To this end, we reorganize the convolution of the $\mathcal{T}^{[ij]}$ amplitudes with the GPDs (the convolution with the symmetric DA being understood) as

$$\left\{ \begin{array}{l} \mathcal{T}_{\text{PP}}^{[ij]} \otimes \tilde{H}^q \\ \mathcal{T}_{\text{SP}}^{[ij]} \otimes H^q \end{array} \right\} : (e_i - e_j)^2 \left\{ \begin{array}{l} \mathcal{T}_X^{(+)} \otimes \frac{\tilde{H}^{q(+)}}{2} \\ \mathcal{T}_{X5}^{(+)} \otimes \frac{H^{q(+)}}{2} \end{array} \right\} + (e_i^2 - e_j^2) \left\{ \begin{array}{l} \mathcal{T}_X^{(-)} \otimes \frac{\tilde{H}^{q(-)}}{2} \\ \mathcal{T}_{X5}^{(-)} \otimes \frac{H^{q(-)}}{2} \end{array} \right\} + e_i e_j \left\{ \begin{array}{l} \mathcal{T}_X^{(0)} \otimes \frac{\tilde{H}^{q(+)}}{2} \\ \mathcal{T}_{X5}^{(0)} \otimes \frac{H^{q(+)}}{2} \end{array} \right\} \quad (2.49)$$

⁸Note that in this study we adopt the convention for T_{B5} which is opposite both [8] and [9].

multiplied by corresponding tensor structures $T_{X(5)}$, where $X \in \{A, B\}$, while $\mathcal{T}_{X(5)}^{(+)}$, $\mathcal{T}_{X(5)}^{(-)}$, and $\mathcal{T}_{X(5)}^{(0)}$ are defined through

$$\frac{1}{2} \left(\mathcal{T}_{X(5)}^{(i)} + \mathcal{T}_{X(5)}^{(j)} \right) \rightarrow \mathcal{T}_{X(5)}^{(+)}, \quad \frac{1}{2} \left(\mathcal{T}_{X(5)}^{(i)} - \mathcal{T}_{X(5)}^{(j)} \right) \rightarrow \mathcal{T}_{X(5)}^{(-)}, \quad \mathcal{T}_{X(5)}^{(i)} + \mathcal{T}_{X(5)}^{(j)} + \mathcal{T}_{X(5)}^{(ij)} \rightarrow \mathcal{T}_{X(5)}^{(0)}. \quad (2.50)$$

By further exploiting the symmetry properties of the DA and GPDs (hence the notation \rightarrow), we simplify $\mathcal{T}_{X(5)}^{(+)}$, $\mathcal{T}_{X(5)}^{(-)}$, and $\mathcal{T}_{X(5)}^{(0)}$. The resulting compact analytical expressions are summarized in Table 1.

The gluonic subprocess $\gamma(q\bar{q}) \rightarrow \gamma(gg)$ contributes to photon-meson photoproduction via the flavour-singlet channel. Its amplitude is obtained from 24 Feynman diagrams, six of which are displayed in Fig. 4, and the remaining ones follow from $(z \rightarrow \bar{z})$, $(y \rightarrow \bar{y})$, and $(y, z) \rightarrow (\bar{y}, \bar{z})$ exchanges. The total amplitude takes the form

$$\mathcal{T}_{\text{PP}}^{[gg]} = \left\{ e_q^2 \left(\mathcal{T}_A^{[gg]} T_A + \mathcal{T}_B^{[gg]} T_B \right) \right\} + \{(y \rightarrow \bar{y})\} - \{(z \rightarrow \bar{z})\} - \{(y, z) \rightarrow (\bar{y}, \bar{z})\}, \quad (2.51)$$

and

$$\mathcal{T}_{\text{SP}}^{[gg]} = \left\{ e_q^2 \left(\mathcal{T}_{A5}^{[gg]} T_{A5} + \mathcal{T}_{B5}^{[gg]} T_{B5} \right) \right\} - \{(y \rightarrow \bar{y})\} - \{(z \rightarrow \bar{z})\} + \{(y, z) \rightarrow (\bar{y}, \bar{z})\}, \quad (2.52)$$

which leads to

$$\mathcal{T}_{\text{PP}}^{[gg]}(y, z) = -\mathcal{T}_{\text{PP}}^{[gg]}(\bar{y}, \bar{z}), \quad \mathcal{T}_{\text{SP}}^{[gg]}(y, z) = \mathcal{T}_{\text{SP}}^{[gg]}(\bar{y}, \bar{z}). \quad (2.53)$$

These symmetry relations, together with the antisymmetric nature of the gluon distribution amplitude (2.31), select in the convolution only those GPDs with definite symmetry properties (2.42):

$$\left\{ \begin{array}{c} \mathcal{T}_{\text{PP}}^{[gg]} \otimes \frac{y}{2} \tilde{H}^q \\ \mathcal{T}_{\text{SP}}^{[gg]} \otimes \frac{y}{2} H^q \end{array} \right\} \otimes \phi_{\eta_{1g}} = e_q^2 \left\{ \begin{array}{c} \mathcal{T}_A^{(g)} \otimes \frac{y}{2} \tilde{H}^{q(+)} T_A \\ \mathcal{T}_{A5}^{(g)} \otimes \frac{y}{2} H^{q(+)} T_{A5} \end{array} \right\} \otimes \phi_{\eta_{1g}} + e_q^2 \left\{ \begin{array}{c} \mathcal{T}_B^{(g)} \otimes \frac{y}{2} \tilde{H}^{q(+)} T_B \\ \mathcal{T}_{B5}^{(g)} \otimes \frac{y}{2} H^{q(+)} T_{B5} \end{array} \right\} \otimes \phi_{\eta_{1g}}. \quad (2.54)$$

Making further use of the DA and GPD symmetry relations, we obtain a concise analytical forms for $\mathcal{T}_{X(5)}^{(g)}$, which are presented in Table 1.

Relations analogous to (2.49) and (2.54) apply also to \tilde{E}^q and E^q . While all terms from (2.49) contribute to $\gamma\pi^\pm$ photoproduction, only the $\mathcal{T}_{X(5)}^{(0)}$ terms contribute to the photoproduction of neutral mesons. In the flavour-singlet channel, i.e., for $\gamma\eta_1$ photoproduction, the $\mathcal{T}_{X(5)}^{(g)}$ terms contribute as well.

Structure of the subprocess amplitudes - As seen from Table 1, the building blocks of the subprocess amplitudes for $\gamma(q_1\bar{q}_2) \rightarrow \gamma(q_1\bar{q}_2)$ and $\gamma(q\bar{q}) \rightarrow \gamma(gg)$ reduce, after using the symmetry properties of the GPD and DA, to

$$\frac{1}{z}, \quad \frac{1}{y \pm i\epsilon}, \quad \frac{f(z)}{\bar{z}y - \alpha z\bar{y} + i\epsilon}. \quad (2.55)$$

The first two terms convey moment-type information on DAs and GPDs, which also appear at LO in the meson transition form factor and in DVCS, as well as in the meson electromagnetic form factor and in DVMP. Note that the NLO corrections to these processes provide additional insight into the behavior of GPDs and DAs beyond the moment-type approximation. The $\pm i\epsilon$ designations appearing in our results reflect the presence of timelike and spacelike scales. The third term in (2.55), i.e., the "mixed" contributions appearing in $\mathcal{T}_{A(5)}^{(0)}$ and $\mathcal{T}_{B(5)}^{(0)}$, in principle already at LO, reveals further information on DAs and GPDs, as it introduces an external scale into the propagators. The same building blocks also

appear in the analytical expressions for amplitudes evaluated in different photon gauges.

Principal Value (PV) representation - Using Eqs. (D.1) and (D.4), the functions $\mathcal{T}_{X(5)}$ from Table 1 can be expressed in the principal-value and δ -function representations, as listed in Table 2. This form is convenient for numerical implementation and subsequent integration, as detailed in Appendix D. In this representation, one clearly separates real and imaginary parts, allowing for a more transparent analysis of the relative contribution sizes. The $\delta(y)$ terms vanish for the $\gamma M' \rightarrow \gamma M$ case, i.e. for pion-pole contributions, since \tilde{E}_{pole} is expressed in terms of pion DA which vanishes at the end points. When convoluted with other GPDs, these terms can be sizable and correspond to the GPD values at $x = \pm\xi$, thus carrying the same cross-over line information as obtained in LO DVCS and DVMP. The "mixed" terms are those that make a difference, although their numerical impact is less pronounced.

2.5 Compton-meson form factors in selected channels

In the preceding sections we have introduced all the necessary elements for determining the Compton-meson form factors defined in Sec. 2.2, Eqs. (2.20-2.23). The quark contribution to the Compton-meson form factor for the process $\gamma N \rightarrow \gamma M N'$ ($M \in \{\pi^\pm, \pi^0, \eta_8, \eta_1\}$) is generally expressed as

$$\begin{aligned} & \tilde{\mathcal{H}}_{M;NN'}(\xi, t, s', \alpha; \mu_R, \mu_F) \\ &= N_M(\mu_R) \left(\sum_{i,j,k} \left(\mathcal{C}_M^{ij} f_{NN'}^{ik} \right) \tilde{H}^k(x, \xi, t; \mu_F) \otimes^x \mathcal{T}_{PP}^{[ij]}(x, \xi, z; s', \alpha) \otimes^z \phi_M(z; \mu_F) \right), \end{aligned} \quad (2.56)$$

with the normalization factor

$$N_M(\mu_R) = -\pi^2 \alpha \alpha_s(\mu_R) \frac{C_F f_M}{N_c}, \quad (2.57)$$

where \mathcal{C}_M^{ij} is defined in Eq. (2.29), and the functions $f_{NN'}^{ij}$ are process-dependent and encode isospin symmetry:

$$\begin{aligned} f_{pn}^{uk} &= \delta^{ku} - \delta^{kd}, & f_{np}^{dk} &= \delta^{ku} - \delta^{kd}, \\ f_{pp}^{ik} &= \delta^{ik}, & f_{nn}^{ik} &= \delta^{iu} \delta^{kd} + \delta^{id} \delta^{ku} + \delta^{is} \delta^{ks}. \end{aligned} \quad (2.58)$$

The convolution $\tilde{H}^k \otimes \mathcal{T}_{PP}^{[ij]}$ is to be replaced by the symmetrized forms defined in (2.49), employing the building blocks summarized in Table 1. The gluon contribution to the Compton-meson form factor for the process $\gamma N \rightarrow \gamma \eta_{1g} N$ reads

$$\begin{aligned} & \tilde{\mathcal{H}}_{\eta_{1g};NN}(\xi, t, s', \alpha; \mu_R, \mu_F) \\ &= N_{\eta_1}(\mu_R) \left(\sum_k f_{NN}^{ik} \frac{\tilde{H}^{k(+)}(x, \xi, t; \mu_F)}{2} \otimes^x e_i^2 \mathcal{T}_{PP}^{(g)}(x, \xi, z; s', \alpha) \otimes^z \phi_{\eta_{1g}}(z; \mu_F) \right). \end{aligned} \quad (2.59)$$

The components of $\mathcal{T}^{(g)}$ corresponding to the decomposition (2.54) are given in Table 1. Analogous expressions hold for $\tilde{\mathcal{E}}$ as well as for the vector CMFFs, \mathcal{H} and \mathcal{E} , evaluated using \mathcal{T}_{SP} .

It is convenient to introduce combinations of GPDs that naturally arise in the calculation of specific photoproduction channels of interest, namely $\gamma p \rightarrow \gamma \pi^+ n$, $\gamma n \rightarrow \gamma \pi^- p$, $\gamma p \rightarrow \gamma \pi^0 p$, $\gamma p \rightarrow \gamma \eta p$, and

Table 1: Functions $\mathcal{T}_{X^{(5)}}$ ($X \in \{A, B\}$) contributing to the subprocess amplitudes $\gamma(q_1\bar{q}_2) \rightarrow \gamma(q_1\bar{q}_2)$ (2.49) and $\gamma(q\bar{q}) \rightarrow \gamma(gg)$ (2.54).

	A	B
$\mathcal{T}_X^{(+)}$	$\frac{4}{s' \alpha \bar{\alpha} z} \left(\frac{\alpha(2\alpha - 1)}{y + i\epsilon} + \frac{1 + (\alpha - 3)(2\alpha - 1)}{y - i\epsilon} \right)$	$\frac{-8}{s'^2 \alpha^2 \bar{\alpha} z} \left(\frac{\alpha}{y + i\epsilon} + \frac{\alpha - 2}{y - i\epsilon} \right)$
$\mathcal{T}_X^{(-)}$	$\frac{4}{s' \bar{\alpha} z} \left(\frac{2\alpha - 1}{y + i\epsilon} - \frac{2\alpha - 5}{y - i\epsilon} \right)$	$\frac{-8}{s'^2 \alpha \bar{\alpha} z} \left(\frac{1}{y + i\epsilon} - \frac{1}{y - i\epsilon} \right)$
$\mathcal{T}_X^{(0)}$	$\frac{8}{s' \alpha} \left(\frac{2\alpha - 1}{\bar{\alpha} z (y + i\epsilon)} - \frac{2\alpha - 1 - \bar{\alpha}^2}{\bar{\alpha} z (y - i\epsilon)} - \frac{(\bar{z} + \alpha z)^2 + \alpha}{z\bar{z}(\bar{z}y - \alpha z\bar{y} + i\epsilon)} \right)$	$\frac{-16}{s'^2 \alpha^2 \bar{\alpha} z} \left(\frac{1}{y + i\epsilon} - \frac{1}{y - i\epsilon} \right)$
$\mathcal{T}_X^{(g)}$	$\frac{8}{s' \alpha \bar{\alpha}} \left(\frac{2\alpha - 1}{z^2 (y + i\epsilon)} + \frac{1}{z^2 (y - i\epsilon)} - \frac{(z + \alpha\bar{z})(\bar{z} + \alpha z)^2}{z^2 \bar{z}^2 (\bar{z}y - \alpha z\bar{y} + i\epsilon)} \right)$	$\frac{-16}{s'^2 \alpha^2 \bar{\alpha} z^2} \left(\frac{1}{y + i\epsilon} - \frac{1}{y - i\epsilon} \right)$
	A5	B5
$\mathcal{T}_{X5}^{(+)}$	$\frac{16\xi i}{s'^3 \alpha^2 \bar{\alpha}^2 z} \left(\frac{\alpha}{y + i\epsilon} + \frac{3\alpha - 4}{y - i\epsilon} \right)$	$\frac{-16\xi i}{s'^3 \alpha \bar{\alpha}^2 z} \left(\frac{2\alpha - 1}{y + i\epsilon} + \frac{2\alpha - 3}{y - i\epsilon} \right)$
$\mathcal{T}_{X5}^{(-)}$	$\frac{16\xi i}{s'^3 \alpha \bar{\alpha}^2 z} \left(\frac{1}{y + i\epsilon} - \frac{1}{y - i\epsilon} \right)$	$\frac{-16\xi i(2\alpha - 1)}{s'^3 \alpha \bar{\alpha}^2 z} \left(\frac{1}{y + i\epsilon} - \frac{1}{y - i\epsilon} \right)$
$\mathcal{T}_{X5}^{(0)}$	$\frac{32\xi i}{s'^3 \alpha^2} \left(\frac{1}{\bar{\alpha}^2 z (y + i\epsilon)} + \frac{\alpha^2 - 2}{\bar{\alpha}^2 z (y - i\epsilon)} - \frac{\alpha z^2 - \bar{z}^2}{z\bar{z}(\bar{z}y - \alpha z\bar{y} + i\epsilon)} \right)$	$-\mathcal{T}_{A5}^{(0)}(y, z) + \mathcal{T}_{\Delta B5}^{(0)}(y, z)$
		$\mathcal{T}_{\Delta B5}^{(0)} = \frac{64\xi i}{s'^3 \alpha^2 \bar{\alpha} z} \left(\frac{1}{y + i\epsilon} - \frac{1}{y - i\epsilon} \right)$
$\mathcal{T}_{X5}^{(g)}$	$\frac{32\xi i}{s'^3 \alpha^2 \bar{\alpha}^2} \left(\frac{1}{z^2 (y + i\epsilon)} - \frac{1}{z^2 (y - i\epsilon)} - \frac{(\bar{z} + \alpha z)(\alpha - \bar{\alpha}^2 z\bar{z})}{z^2 \bar{z}^2 (\bar{z}y - \alpha z\bar{y} + i\epsilon)} \right)$	$-\mathcal{T}_{A5}^{(g)}(y, z) + \mathcal{T}_{\Delta B5}^{(g)}(y, z)$
		$\mathcal{T}_{\Delta B5}^{(g)} = \frac{64\xi i}{s'^3 \alpha^2 \bar{\alpha} z^2} \left(\frac{1}{y + i\epsilon} - \frac{1}{y - i\epsilon} \right)$

Table 2: Principal-value and δ -function representations of the functions $\mathcal{T}_{X^{(5)}}$ ($X \in \{A, B\}$) listed in Table 1, which contribute to the subprocess amplitudes $\gamma(q_1\bar{q}_2) \rightarrow \gamma(q_1\bar{q}_2)$ (2.49) and $\gamma(q\bar{q}) \rightarrow \gamma(gg)$ (2.54).

	A	B
$\mathcal{T}_X^{(+)}$	$\frac{8}{s'z} \left(\frac{2\bar{\alpha}}{\alpha} \mathcal{P} \frac{1}{y} - i\pi \frac{3\alpha - 2}{\alpha\bar{\alpha}} \delta(y) \right)$	$\frac{16}{s'^2 z} \left(\frac{1}{\alpha^2} \mathcal{P} \frac{1}{y} + i\pi \frac{1}{\alpha^2\bar{\alpha}} \delta(y) \right)$
$\mathcal{T}_X^{(-)}$	$\frac{8}{s'z} \left(\frac{2}{\bar{\alpha}} \mathcal{P} \frac{1}{y} - i\pi \frac{2\alpha - 3}{\bar{\alpha}} \delta(y) \right)$	$\frac{16i\pi \delta(y)}{s'^2 \alpha\bar{\alpha} z}$
$\mathcal{T}_X^{(0)}$	$\frac{8}{s'} \left[\frac{\bar{\alpha}}{\alpha z} \mathcal{P} \frac{1}{y} + i\pi \frac{\bar{\alpha}^2 - 2(2\alpha - 1)}{\alpha\bar{\alpha} z} \delta(y) \right.$ $\left. + \frac{\alpha + (\bar{z} + \alpha z)^2}{\alpha z \bar{z} (y + \alpha\bar{y})} \left(\mathcal{P} \left(\frac{1}{z - \frac{y}{y + \alpha\bar{y}}} \right) + i\pi \delta \left(z - \frac{y}{y + \alpha\bar{y}} \right) \right) \right]$	$\frac{32i\pi \delta(y)}{s'^2 \alpha^2 \bar{\alpha} z}$
$\mathcal{T}_X^{(g)}$	$\frac{8}{s'} \left[\frac{2}{\bar{\alpha} z^2} \mathcal{P} \frac{1}{y} + i\pi \frac{2}{\alpha z^2} \delta(y) \right.$ $\left. + \frac{(z + \alpha\bar{z})(\bar{z} + \alpha z)^2}{\alpha\bar{\alpha} z^2 \bar{z}^2 (y + \alpha\bar{y})} \left(\mathcal{P} \left(\frac{1}{z - \frac{y}{y + \alpha\bar{y}}} \right) + i\pi \delta \left(z - \frac{y}{y + \alpha\bar{y}} \right) \right) \right]$	$\frac{32i\pi \delta(y)}{s'^2 \alpha^2 \bar{\alpha} z^2}$
	A5	B5
$\mathcal{T}_{X5}^{(+)}$	$\frac{-32\xi i}{s'^3 z} \left(\frac{2}{\alpha^2 \bar{\alpha}} \mathcal{P} \frac{1}{y} + i\pi \frac{2 - \alpha}{\alpha^2 \bar{\alpha}^2} \delta(y) \right)$	$\frac{32\xi i}{s'^3 z} \left(\frac{2}{\alpha\bar{\alpha}} \mathcal{P} \frac{1}{y} + i\pi \frac{1}{\alpha\bar{\alpha}^2} \delta(y) \right)$
$\mathcal{T}_{X5}^{(-)}$	$\frac{-32\xi i}{s'^3 \alpha \bar{\alpha}^2 z} i\pi \delta(y)$	$\frac{32\xi i (2\alpha - 1)}{s'^3 \alpha \bar{\alpha}^2 z} i\pi \delta(y)$
$\mathcal{T}_{X5}^{(0)}$	$\frac{-32\xi i}{s'^3} \left[\frac{1 + \alpha}{\alpha^2 \bar{\alpha} z} \mathcal{P} \frac{1}{y} + i\pi \frac{(3 - \alpha^2)}{\alpha^2 \bar{\alpha}^2 z} \delta(y) \right.$ $\left. + \frac{\bar{z}^2 - \alpha z^2}{\alpha^2 z \bar{z} (y + \alpha\bar{y})} \left(\mathcal{P} \left(\frac{1}{z - \frac{y}{y + \alpha\bar{y}}} \right) + i\pi \delta \left(z - \frac{y}{y + \alpha\bar{y}} \right) \right) \right]$	$-\mathcal{T}_{A5}^{(0)}(y, z) + \frac{-128\xi i}{s'^3 \alpha^2 \bar{\alpha} z} i\pi \delta(y)$
$\mathcal{T}_{X5}^{(g)}$	$\frac{-32\xi i}{s'^3} \left[i\pi \frac{2}{\alpha^2 \bar{\alpha}^2 z^2} \delta(y) \right.$ $\left. + \frac{(\bar{z} + \alpha z)(\bar{\alpha}^2 z \bar{z} - \alpha)}{\alpha^2 \bar{\alpha}^2 z^2 \bar{z}^2 (y + \alpha\bar{y})} \left(\mathcal{P} \left(\frac{1}{z - \frac{y}{y + \alpha\bar{y}}} \right) + i\pi \delta \left(z - \frac{y}{y + \alpha\bar{y}} \right) \right) \right]$	$-\mathcal{T}_{A5}^{(g)}(y, z) + \frac{-128\xi i}{s'^3 \alpha^2 \bar{\alpha} z^2} i\pi \delta(y)$

$\gamma p \rightarrow \gamma \eta' p$:

$$\begin{aligned}\tilde{H}_{\pi^\pm} &= \tilde{H}^u - \tilde{H}^d, & \tilde{H}_{\pi^0} &= \frac{1}{\sqrt{2}} \left(e_u^2 \tilde{H}^u - e_d^2 \tilde{H}^d \right), \\ \tilde{H}_{\eta_8} &= \frac{1}{\sqrt{6}} \left(e_u^2 \tilde{H}^u + e_d^2 \tilde{H}^d - 2e_s^2 \tilde{H}^s \right), & \tilde{H}_{\eta_1} &= \frac{1}{\sqrt{3}} \left(e_u^2 \tilde{H}^u + e_d^2 \tilde{H}^d + e_s^2 \tilde{H}^s \right),\end{aligned}\quad (2.60)$$

and analogously for \tilde{E} , H , and E GPDs. The CMFFs for $\gamma\pi^+$ photoproduction then read

$$\tilde{\mathcal{H}}_{\pi^+} = N_\pi \tilde{H}_{\pi^\pm} \otimes^x \mathcal{T}_{\text{PP}}^{[ud]} \otimes^z \phi_\pi, \quad \mathcal{H}_{\pi^+} = N_\pi H_{\pi^\pm} \otimes^x \mathcal{T}_{\text{SP}}^{[ud]} \otimes^z \phi_\pi, \quad (2.61)$$

while for $\gamma\pi^-$ photoproduction, $\mathcal{T}^{[ud]}$ is replaced by $\mathcal{T}^{[du]}$. In both cases, the symmetrized expressions of (2.49) are employed. For the neutral flavour-octet mesons π^0 and η_8 , the CMFFs take the form

$$\tilde{\mathcal{H}}_{\pi^0} = N_\pi \frac{\tilde{H}_{\pi^0}^{(+)}}{2} \otimes^x \mathcal{T}_{\text{PP}}^{(0)} \otimes^z \phi_\pi, \quad \mathcal{H}_{\pi^0} = N_\pi \frac{H_{\pi^0}^{(+)}}{2} \otimes^x \mathcal{T}_{\text{SP}}^{(0)} \otimes^z \phi_\pi, \quad (2.62)$$

and

$$\tilde{\mathcal{H}}_{\eta_8} = N_{\eta_8} \frac{\tilde{H}_{\eta_8}^{(+)}}{2} \otimes^x \mathcal{T}_{\text{PP}}^{(0)} \otimes^z \phi_{\eta_8}, \quad \mathcal{H}_{\eta_8} = N_{\eta_8} \frac{H_{\eta_8}^{(+)}}{2} \otimes^x \mathcal{T}_{\text{SP}}^{(0)} \otimes^z \phi_{\eta_8}. \quad (2.63)$$

The CMFFs for the flavour-singlet η_1 meson consist of both quark and gluon contributions:

$$\begin{aligned}\tilde{\mathcal{H}}_{\eta_1} &= N_{\eta_1} \frac{\tilde{H}_{\eta_1}^{(+)}}{2} \otimes^x \left(\mathcal{T}_{\text{PP}}^{(0)} \quad \mathcal{T}_{\text{PP}}^{(g)} \right) \otimes^z \begin{pmatrix} \phi_{\eta_1} \\ \phi_{\eta_{1g}} \end{pmatrix}, \\ \mathcal{H}_{\eta_1} &= N_{\eta_1} \frac{H_{\eta_1}^{(+)}}{2} \otimes^x \left(\mathcal{T}_{\text{SP}}^{(0)} \quad \mathcal{T}_{\text{SP}}^{(g)} \right) \otimes^z \begin{pmatrix} \phi_{\eta_1} \\ \phi_{\eta_{1g}} \end{pmatrix},\end{aligned}\quad (2.64)$$

which mix under DA evolution. Finally, the CMFFs of the physical states, i.e., the η and η' mesons, are obtained through phenomenological mixing (2.37-2.39):

$$\begin{aligned}\tilde{\mathcal{H}}_\eta &= \cos \theta_8 \tilde{\mathcal{H}}_{\eta_8} - \sin \theta_1 \tilde{\mathcal{H}}_{\eta_1}, \\ \tilde{\mathcal{H}}_{\eta'} &= \sin \theta_8 \tilde{\mathcal{H}}_{\eta_8} + \cos \theta_1 \tilde{\mathcal{H}}_{\eta_1}.\end{aligned}\quad (2.65)$$

Analogous relations hold for the other CMFFs not shown explicitly.

3 Observables

In the numerical analysis presented in this work, we examine the cross sections, focusing on their fully differential, single-differential, and integrated forms.

3.1 Fully differential cross-section

The fully differential cross section for the $\gamma N \rightarrow \gamma MN'$ process is given by

$$\frac{d\sigma}{ds' d(-t) d\alpha} = \frac{|\overline{\mathcal{M}}|^2}{32S_{\gamma N}^2 (2\pi)^3}, \quad (3.1)$$

where

$$|\overline{\mathcal{M}}|^2 = |\overline{\mathcal{M}}^{\text{PP}}|^2 + |\overline{\mathcal{M}}^{\text{SP}}|^2 \quad (3.2)$$

denotes the squared amplitude \mathcal{M} (2.20), summed over nucleon helicities and photon polarizations, and averaged over the polarizations of the incoming particles. Due to the QED Ward identities,

$$\sum_{\lambda_q, \lambda_k} |\mathcal{M}^{\text{PP}}(\lambda_q, \lambda_k)|^2 = \mathcal{M}^{\text{PP} \mu\nu} \mathcal{M}_{\mu\nu}^{\text{PP}*}, \quad \sum_{\lambda_q, \lambda_k} |\mathcal{M}^{\text{SP}}(\lambda_q, \lambda_k)|^2 = \mathcal{M}^{\text{SP} \mu\nu} \mathcal{M}_{\mu\nu}^{\text{SP}*}. \quad (3.3)$$

Using the standard spinor-sum identities with bilinears (2.19), and taking into account (2.24-2.27), one obtains

$$\begin{aligned} |\overline{\mathcal{M}}^{\text{PP}}|^2 = & 2 \left[(1 - \xi^2) \left(2 |\tilde{\mathcal{H}}_A|^2 - 2s'\alpha\bar{\alpha} \operatorname{Re}(\tilde{\mathcal{H}}_A \tilde{\mathcal{H}}_B^*) + s'^2 \alpha^2 \bar{\alpha}^2 |\tilde{\mathcal{H}}_B|^2 \right) \right. \\ & - 2\xi^2 \left(2 \operatorname{Re}(\tilde{\mathcal{H}}_A \tilde{\mathcal{E}}_A^*) - s'\alpha\bar{\alpha} \operatorname{Re}(\tilde{\mathcal{H}}_A \tilde{\mathcal{E}}_B^* + \tilde{\mathcal{E}}_A \tilde{\mathcal{H}}_B^*) + s'^2 \alpha^2 \bar{\alpha}^2 \operatorname{Re}(\tilde{\mathcal{H}}_B \tilde{\mathcal{E}}_B^*) \right) \\ & \left. - \frac{\xi^2 t}{4m_{\text{N}}^2} \left(2 |\tilde{\mathcal{E}}_A|^2 - 2s'\alpha\bar{\alpha} \operatorname{Re}(\tilde{\mathcal{E}}_A \tilde{\mathcal{E}}_B^*) + s'^2 \alpha^2 \bar{\alpha}^2 |\tilde{\mathcal{E}}_B|^2 \right) \right], \quad (3.4) \end{aligned}$$

and

$$\begin{aligned} |\overline{\mathcal{M}}^{\text{SP}}|^2 = & \frac{s'^4 \alpha^2 \bar{\alpha}^2}{8\xi^2} \left[(1 - \xi^2) \left(|\mathcal{H}_{A5}|^2 + |\mathcal{H}_{B5}|^2 \right) - 2\xi^2 \left(\operatorname{Re}(\mathcal{H}_{A5} \mathcal{E}_{A5}^* + \mathcal{H}_{B5} \mathcal{E}_{B5}^*) \right) \right. \\ & \left. - \left(\xi^2 + \frac{t}{4m_{\text{N}}^2} \right) \left(|\mathcal{E}_{A5}|^2 + |\mathcal{E}_{B5}|^2 \right) \right]. \quad (3.5) \end{aligned}$$

Note that there is no interference between parity-odd ($\tilde{\mathcal{H}}, \tilde{\mathcal{E}}$) and parity-even (\mathcal{H}, \mathcal{E}) CMFFs.

3.2 Single differential and integrated cross-sections

To determine the single-differential and integrated cross sections, special care must be taken regarding the cuts in the phase-space plane $(-t, \alpha)$, or equivalently $(-t, -u')$. This procedure was discussed in detail in [8, 9]; here we summarize the main points. The common lower limit for t is obtained from (A.4):

$$(-t)_{\min} \equiv (-t_0) = \frac{4\xi^2 m_{\text{N}}^2}{1 - \xi^2}. \quad (3.6)$$

According to the factorization conditions, $(-t)$ must remain small, while, apart from s' , both $(-u')$ and $(-t')$ should be large, i.e., $-u', -t' \gg \Lambda_{\text{QCD}}$. In the language of [20, 25], this corresponds to large $|\kappa_{\perp}|$. As was demonstrated in [22], the imposed cuts on the Mandelstam invariants ensure that this is the case. We therefore adopt the choice

$$(-t)_{\max} = 0.5 \text{ GeV}^2, \quad (-u')_{\min} = (-t')_{\min} = 1 \text{ GeV}^2. \quad (3.7)$$

These values guarantee $M_{\gamma\text{M}}^2 > 1.5 \text{ GeV}^2$ and ensure that the kinematics stay well outside the resonance region in the collinear limit [22]. From (2.3) one obtains $(-u')$ as a function of $(-t)$:

$$(-u')[-t] = (-t) + s' - (-t')_{\min} - m_{\text{M}}^2. \quad (3.8)$$

The corresponding maximum value is

$$(-u')_{\max} = s' + (-t)_{\max} - (-t')_{\min} - m_M^2. \quad (3.9)$$

Consequently, the allowed kinematical domain for $(-u')$ is $(-u')_{\min} < (-u') < (-u')_{\max}$, while the corresponding α limits are derived from (2.13).

The single-differential cross section can be written in the form

$$\begin{aligned} \frac{d\sigma}{d\xi} = & \frac{2(S_{\gamma N} - m_N^2)}{(1 + \xi)^2} \left(\Theta(s'_{\text{Min}} \leq s' \leq s'_{\text{Trans}}) \int_{(-t)_{[\alpha_{\min}]}}^{(-t)_{\max}} d(-t) \int_{\alpha_{\min}}^{\alpha[-t]} d\alpha \right. \\ & \left. + \Theta(s'_{\text{Trans}} \leq s' \leq s'_{\text{Max}}) \int_{(-t)_{\min}}^{(-t)_{\max}} d(-t) \int_{\alpha_{\min}}^{\alpha[-t]} d\alpha \right) \frac{d\sigma}{ds' d(-t) d\alpha}. \end{aligned} \quad (3.10)$$

Here we introduce $\alpha[-t]$, which follows from (3.8), and its inverse, $(-t)[\alpha]$. This representation is more compact than the corresponding expression in Refs. [8, 9], as in our case both the α and t integrations are performed numerically. The integration order was selected to yield a concise and computationally convenient form for numerical evaluation. From (2.3) one finds

$$s'_{\text{Min}} = (-u')_{\min} + (-t')_{\min} + m_M^2 - (-t)_{\max}, \quad (3.11)$$

which, combined with (2.6), defines the lower kinematic limit $\xi_{\text{Min}}(S_{\gamma N}, m_M^2)$. The transition point s'_{Trans} follows from the condition $(-u')_{\min} = (-u')[(-t)_{\min}]$, resulting in a lengthy analytical expression that depends on $S_{\gamma N}$, m_N , m_M , and on the parameter choices given in (3.7). The upper limit, s'_{Max} , is obtained for $(-t)_{\min} = (-t)_{\max}$:

$$s'_{\text{Max}} = \frac{S_{\gamma N} - m_N^2}{2m_N^2} \left(-(-t)_{\max} + \sqrt{(-t)_{\max}^2 + 4m_N^2(-t)_{\max}} \right), \quad (3.12)$$

which corresponds to

$$\xi_{\text{Max}} = \sqrt{\frac{(-t)_{\max}}{4m_N^2 + (-t)_{\max}}}, \quad (3.13)$$

and for the parameter choice of (3.7) gives $\xi_{\text{Max}} = 0.3526$. The lower limit $(S_{\gamma N})_{\min}$ is fixed by the condition $s'_{\text{Min}} = s'_{\text{Max}}$, and depends on the nucleon and meson masses, and on the same parameter set.

Integrating (3.10) over ξ yields the total cross section as a function of $S_{\gamma N}$:

$$\sigma = \int_{\xi_{\text{Min}}}^{\xi_{\text{Max}}} d\xi \frac{d\sigma}{d\xi}. \quad (3.14)$$

4 Analysis of numerical results

This section presents the numerical analysis of photon-meson pair photoproduction, $\gamma N \rightarrow \gamma MN'$, for selected pseudoscalar mesons $M \in \{\pi^+, \pi^-, \pi^0, \eta, \eta'\}$. The proton is taken as the target nucleon, except for π^- photoproduction, where the target nucleon is a neutron. The perturbative framework is summarized in Sec. 2, where only the quark GPD contributions are considered. In particular, we make use of our analytical results for the subprocess amplitudes, Table 2, and the integration procedure described in App. D. The nonperturbative inputs, namely the GPDs and DAs, are discussed in Sec. 2.3.

Our numerical analysis focuses on the moderate- ξ region ($\xi > 0.1$). We use the GK model [31, 32, 51], and the valence quark approximation⁹. In addition, the π -pole contribution governed by \tilde{E}_{pole} (2.43) is included, as it is expected to play an important role in this kinematic domain. For pions, several DA shapes are tested, defined either via the truncated Gegenbauer expansion (2.32) or via the beta-function ansatz: the asymptotic form $\phi_{\pi, \text{as}}, \phi_{\pi, [0.116]}$ (2.34), and the broader parameterizations $\phi_{\pi}^{(0.5)}, \phi_{\pi}^{(0.4)}$, and $\phi_{\pi}^{(0.3)}$ (2.35). The η and η' mesons are described in the octet-singlet basis using $\phi_{\eta_8}, \phi_{\eta_1=\eta_{1q}}$, and the gluon DA $\phi_{\eta_{1g}}$ (2.33). Their Gegenbauer coefficients follow (2.36), and the decay-constant mixing (2.37) is implemented. DA evolution is performed according to Eqs. (B.4-B.10), and the strong coupling constant is evaluated at LO:

$$\alpha_s(\mu) = \frac{4\pi}{\beta_0 \log(\mu^2/\Lambda_{\text{QCD}}^2)}, \quad \beta_0 = 11 - \frac{2}{3} \tilde{n}_f. \quad (4.1)$$

We take $\tilde{n}_f = 4$ and $\Lambda_{\text{QCD}} = 0.22 \text{ GeV}$,¹⁰ corresponding to four active flavours at the relevant scales. The observables analyzed in this section - defined previously in Sec. 3 - are the fully differential cross section (3.1), the single differential cross section (3.10), and the total cross section (3.14).

There are several key aspects of the analysis that we aim to address in this section:

- We assess the relative importance of \tilde{H}, \tilde{E}, H , and E GPDs, i.e., of $\tilde{\mathcal{H}}, \tilde{\mathcal{E}}, \mathcal{H}$, and \mathcal{E} Compton-meson form factors, and in particular the role of \tilde{E}_{pole} , i.e., the π -pole contribution $\tilde{\mathcal{E}}_{\text{pole}}$.
- We investigate the dependence of our predictions on the meson structure. For pions, several DA shapes are tested. For η and η' mesons, we put special emphasis on highlighting the role of two-gluon contributions. We also examine the sensitivity on the choice of factorization scale μ_F .
- We study the dependence of our LO predictions on the choice of the renormalization scale μ_R .

To illustrate the dependence on the kinematical conditions relevant for JLab kinematics, we present a comparison of the fully differential cross-section evaluated at $t = t_0$ (3.6) for selected combinations of $(s', S_{\gamma N})$ and the corresponding ξ values determined from (2.6):

$$\begin{aligned} \text{(I)} \quad (s', S_{\gamma N}) &= (4, 20) \text{ GeV}^2 & \xi &= 0.117, & \text{(II)} \quad (s', S_{\gamma N}) &= (4, 9) \text{ GeV}^2 & \xi &= 0.327, \\ \text{(III)} \quad (s', S_{\gamma N}) &= (4, 12) \text{ GeV}^2 & \xi &= 0.219, & \text{(IV)} \quad (s', S_{\gamma N}) &= (7, 20) \text{ GeV}^2 & \xi &= 0.224. \end{aligned} \quad (4.2)$$

Similarly, for the single differential cross section, we compare predictions at $S_{\gamma N} = 6, 10, 20$, and 30 GeV^2 . Unless stated otherwise, as a default choice we use

$$\mu_R^2 = \mu_F^2 = s', \quad \text{and} \quad \phi_{\pi} = \phi_{\pi, [0.116]}, \quad (4.3)$$

the latter corresponding to Eqs. (2.32) and (2.34). Following common practice in large-angle analyses, and taking into account the size of the momentum transfer between the photon and meson (2.16), we also consider the alternative scale

$$\mu^2 = \alpha \bar{\alpha} s', \quad (4.4)$$

for μ_R^2 and μ_F^2 , taken either separately and combined.

For clarity and compactness of presentation, App. E collects all figures: Figs. 5-12 fully differential, Figs. 13-19 single differential, and Figs. 20-22 integrated cross sections and selected ratios.

⁹In this model, only the valence quarks contribute to charged-pion photoproduction, and in the case of neutral mesons we consistently omit both sea-quark and gluon contributions due to the relative importance of valence-quark contributions in this ξ -region, as well as the need for a modified framework when gluons are included.

¹⁰Here, \tilde{n}_f differs from $n_f = 3$, which counts the fixed quark flavours entering the η -meson system.

4.1 GPD contributions and the role of the π pole.

In this work, we include not only the contributions of \tilde{H} and H GPDs, as in [9, 22], but also those of the remaining twist-2 chiral-even GPDs, namely \tilde{E} and E . Since the value of ξ relevant for our analysis is not small, there is no a priori justification for neglecting these terms in (3.4-3.5). Moreover, the t -dependent factors in front of $\tilde{\mathcal{E}}$ and \mathcal{E} in Eqs. (3.4-3.5) enhance the impact of \tilde{E} and E in both single-differential and integrated cross sections, particularly for GPD E . In the fully differential cross section, the role of \tilde{E} is more pronounced than that of E . Still, \mathcal{H} and $\tilde{\mathcal{H}}$ remain the dominant contributions, with the notable exception of $\tilde{\mathcal{E}}_{\text{pole}}$, which is included in our analysis through $\tilde{\mathcal{E}} \rightarrow \tilde{\mathcal{E}} + \tilde{\mathcal{E}}_{\text{pole}}$. Note that the cross section defined in Sec. 3.1 contains interference terms between $\tilde{\mathcal{H}}$ and $\tilde{\mathcal{E}}$, as well as between \mathcal{H} and \mathcal{E} . However, it is obtained as the sum of the partial cross sections, originating from the axial GPDs \tilde{H} and $\tilde{E} + \tilde{E}_{\text{pole}}$, (i.e., $|\mathcal{M}_{\text{PP}}|^2$, (3.4)) and from the vector GPDs H and E (i.e., $|\mathcal{M}_{\text{SP}}|^2$, (3.5)).

Pion-pole in fully differential cross-sections - Figure 5 presents the fully differential cross section as a function of α for the pion, η , and η' mesons, and with the individual GPD contributions clearly identified. The results are evaluated at $t = t_0$ (3.6) and $\xi = 0.117$. The parameter α is related to the photon scattering angle through $\alpha = \cos^2(\theta/2)$ (2.14). Values $\alpha < 0.5$ and $\alpha > 0.5$ correspond to backward and forward kinematics, respectively. Thin lines represent the axial GPD contributions and the total results calculated without including the pion-pole term. In this case, for the $\gamma\pi^+$ channel, the vector GPDs dominate at backward angles, whereas the axial ones dominate at forward angles. For the other channels, the vector contributions, mainly driven by H , dominate throughout the entire α range. Thick solid lines represent the full predictions including \tilde{E}_{pole} . As seen in Fig. 5, the impact of \tilde{E}_{pole} is significant, especially for the π^+ and π^- channels. Unlike DVMP, and analogously to DVCS, the neutral mesons π^0 , η , and η' also receive a contribution from the pion pole. The neutral channels correspond to the $\gamma\pi^0 \rightarrow \gamma M^0$ process, while the charged ones refer to $\gamma\pi^\pm \rightarrow \gamma\pi^\pm$. In both cases, π^0 and π^\pm are described by $\tilde{E}_{\text{pole}} \sim \phi_\pi$ (2.43), which contributes only within the ERBL region.

As already noted in [9], electromagnetic interactions do not preserve isospin symmetry; consequently, $\gamma\pi^+$ and $\gamma\pi^-$ photoproduction differ. At the level of calculation, this difference arises from the lack of definite ($x \rightarrow -x$) symmetry in the contributing GPDs, i.e., from the $(e_i^2 - e_j^2)$ proportional term in (2.49). The pion-pole contributions, however, correspond to charge-conjugated processes $\gamma\pi^\pm \rightarrow \gamma\pi^\pm$ and involve the symmetric \tilde{E}_{pole} GPD. They are therefore equal in magnitude, except for interference with the non-symmetric \tilde{H} .

The π -pole contributions, and consequently the total differential cross section, are enhanced in the $\gamma\pi^\pm$ channel at backward angles ($\alpha < 0.5$ in Fig. 5, i.e., $\cos(\theta) < 0$). A similar backward enhancement is observed in wide-angle Compton scattering on the pion [57, 58, 59, 60], and is attributed to angular momentum conservation¹¹ [57]. The origin of backward dominance in our results can be sketched at a qualitative level. Re-examining the subprocess amplitude decomposition (2.49) together with the results of Table 2, one observes¹² that the terms proportional to $(e_i - e_j)^2$ and $(e_i^2 - e_j^2)$ are predominantly controlled by $1/\alpha = 1/\cos^2(\theta/2)$ and $1/\bar{\alpha} = 1/\sin^2(\theta/2)$, respectively. For the pion-pole contribution in the $\gamma\pi^\pm$ channel, the $(e_i^2 - e_j^2)$ proportional term in (2.49) vanishes, since \tilde{E}_{pole} , expressed through the pion DA, is symmetric under $x \rightarrow -x$. Note that the $\delta(y)$ terms from Table 2 vanish for \tilde{E}_{pole} because the pion DA is zero at the end points. As a result, the $(e_i - e_j)^2$ proportional term in (2.49) enhances the backward-angle region ($\theta \rightarrow \pi$) in the pion-pole contribution to $\gamma\pi^\pm$ production. When the terms

¹¹For a spin-0 meson with helicity-conserving quarks, photon-helicity-flip amplitudes require two units of orbital angular momentum, which are kinematically enhanced near $\theta \rightarrow \pi$.

¹²One should also keep in mind Eqs. (3.4-3.5) with the $\alpha\bar{\alpha}$ factors appearing in the relevant terms.

in Table 2 are convoluted with other GPDs, the $(e_i^2 - e_j^2)$ proportional term in (2.49) also contributes, enhancing the forward-angle region ($\theta \rightarrow 0$) and making the total result more uniform across the α (i.e., θ) range.

Only the third term in (2.49), proportional to $e_i e_j$, contributes to the photoproduction of neutral mesons. Consequently, the pion-pole contribution in neutral-meson production is less pronounced than for charged pions. This observation agrees qualitatively with theoretical and experimental results for the crossed process $\gamma\gamma \rightarrow \pi M$, with the $\sigma(\pi^0\pi^0)/\sigma(\pi^+\pi^-)$ cross-section ratio being ≈ 0.1 theoretically and ≈ 0.3 - 0.5 experimentally [61, 62].

Next, we examine the ξ dependence of the pion-pole contributions. Figure 6 illustrates that the pion-pole contribution to $\gamma\pi^+$ photoproduction is very small (and, interestingly, destructive) for $\xi = 0.01$ at $(s', S_{\gamma N}) = (4, 200)$ GeV², and becomes entirely negligible for $\xi = 0.002$ at $(s', S_{\gamma N}) = (7, 2000)$ GeV². This shows that the pion-pole contribution is indeed small at low ξ , and that the small- ξ predictions given in [9, 22] would not be affected by it.

Figure 7 compares the fully differential cross sections for $\gamma\pi^+$, $\gamma\pi^-$, and $\gamma\pi^0$ final states at four kinematical settings (4.2) with $\xi \in \{0.117, 0.219, 0.224, 0.327\}$. Thin lines represent the results obtained without the π -pole contribution, while thick lines show the full results, allowing us to assess the relative importance of the π -pole term under these conditions. The overall behaviour is similar across all kinematical cases. The $\gamma\pi^-$ cross sections are slightly higher than those for $\gamma\pi^+$, whereas $\gamma\pi^0$ dominates at forward angles. In all cases, the π -pole contribution is very significant for charged pions and remains relevant for π^0 , increasing with ξ . Although ξ is comparable, the predictions for case (IV) are smaller than those for case (III) because of the suppression with $S_{\gamma N}$ in (3.1). Analogously, Figure 8 and Figure 9 compare the fully differential cross sections for $\gamma\eta$ and $\gamma\eta'$ final states at four kinematical settings and for two different choices of μ_R and μ_F . Here too, the pion-pole contributions are sizable and increase with ξ .

Figure 10 illustrates the impact of the pion-pole contributions via the ratio of the fully differential cross section (3.1) calculated with and without \tilde{E}_{pole} for four kinematical settings (4.2) with $\xi \in \{0.117, 0.219, 0.224, 0.327\}$, and for all pseudoscalar mesons considered: π^+ , π^- , π^0 , η , and η' . Since the dependence on $S_{\gamma N}$ and s' cancels, the ratio depends only on ξ and α . The ratio increases with ξ and is large for π^+ and π^- , reaching values between 10 and 60 in the backward region. It is smaller and more symmetric in α for neutral mesons. The ratios for π^0 and η exhibit similar behaviour, with a maximum of around 3 and 1.9, respectively, while the ratio for η' is slightly modified by gg contributions, reaching values up to 2.4. The results for $\xi = 0.219$ (III) and $\xi = 0.224$ (IV) are nearly identical, except for η' , where the gg contribution leads to a small deviation.

Pion-pole in single differential and integrated cross-sections - We now turn to the predictions for the single differential cross section. Figures 13 and 14 show the single differential cross section for $\gamma\pi^+$ and $\gamma\pi^0$ photoproduction evaluated at $S_{\gamma N} = 30, 20, 10,$ and 6 GeV², with the vector and axial-vector GPD contributions indicated as in Fig. 5. A comparison between our results with the pion-pole included (thick lines) and those obtained without the pion-pole term (thin lines for axial and total contributions) illustrates the impact of the pion-pole on this observable. The $\gamma\pi^-$ channel exhibits a similar pattern to $\gamma\pi^+$, but with systematically higher values, and is therefore not shown. Similarly, Figures 15 and 16 present the results for $\gamma\eta$ and $\gamma\eta'$ at $S_{\gamma N} = 10$ and 6 GeV², for two choices of renormalization and factorization scales, (4.3) and (4.4). As discussed for the fully differential cross section, the pion-pole contributions increase with ξ . This is evident from the results at lower $S_{\gamma N}$, where ξ_{min} is already large. Our analysis is not complete at small ξ , and predictions for $\xi \lesssim 0.1$ should therefore be viewed only as

indicative. One observes a pronounced decrease in the total cross section with increasing ξ . Still, the single-differential results confirm that the pion-pole contributions are more important for charged pions, less pronounced but still present for π^0 , η , and η' . To illustrate this effect more clearly, Figure 19 presents the ratio of the single differential cross section obtained with and without the π -pole contribution, for $\gamma\pi^+$ and $\gamma\eta$ photoproduction. The ratio increases with ξ ; for $\xi \in [0.2, 0.3]$ it grows from 3 (1.2) to 8 (1.5) for π^+ (η), at $S_{\gamma N} = 20 \text{ GeV}^2$.

Finally, we discuss the integrated cross-section. Figure 20 presents the cross-sections for the photoproduction of $\gamma\pi^+$, $\gamma\pi^-$, $\gamma\pi^0$, $\gamma\eta$, and $\gamma\eta'$ pairs as functions of the center of mass energy of the incoming photon-nucleon system, $S_{\gamma N}$, for two choices of the renormalization and factorization scales. Thin lines denote the results obtained without the pion-pole contribution. The ratio of the total cross-section with and without the pion-pole contribution, as a function of $S_{\gamma N}$, is displayed in Figure 21. While the pion-pole effects enhance the integrated cross-section less strongly than the differential ones, their impact remains significant for charged pions and still noticeable for light neutral pseudoscalars. For $S_{\gamma N} \in [6, 30] \text{ GeV}^2$, the ratio decreases from about 2-2.5 to 1.4 for charged pions, and from 1.3-1.6 to 1.06 for π^0 , η , and η' .

4.2 Meson structure

Photon-meson photoproduction is sensitive to both the nucleon and meson internal structure.

Pion distribution amplitudes - For $\gamma\pi$ photoproduction, we present predictions based on five pion DAs shown in Fig. 2. Their impact on the fully differential cross-section is illustrated on the left panel of Figure 11, where we show the ratio of the fully differential cross-section for the $\gamma\pi^+$ channel, calculated with a given pion DA and normalized to the result obtained with the asymptotic DA. Thin lines indicate the results obtained without the pion-pole contribution. Corresponding ratios remain nearly constant across the entire α range, taking values of about 1.25 for the default DA $\phi_{[0.116]}$, and up to a factor of 3 for the broadest investigated DA $\phi^{(0.3)}$. When the pion-pole contribution is included, the ratios increase markedly for broader DAs. For $\phi^{(0.3)}$, the ratio ranges from 7.1 to 3.85 across the α interval under consideration. Since the form of \tilde{E}_{pole} (2.43) depends on the pion DA, the resulting backward enhancement is fully consistent with the behaviour described in the preceding subsection. The $\gamma\pi^-$ channel shows the same sensitivity to the DA shape (not shown for brevity), with the broadest DA yielding ratios between 6 and 4, whereas in the $\gamma\pi^0$ channel the ratios are flatter and somewhat lower, around 3 – 3.5.

The right panel of Figure 11 shows the ratio of the full differential cross-sections calculated with and without the pion pole for each DA. This confirms the backward-angle dominance of the charged-pion predictions, which becomes even more pronounced for broader DAs. The $\gamma\pi^-$ channel follows a similar pattern, while for $\gamma\pi^0$ the ratios are somewhat smaller and symmetric in α , as are the corresponding cross-sections themselves.

In the remainder of this work, we use $\phi_{[0.116]}$ as the default DA, whose shape is supported by moment-based lattice results. The numerical predictions obtained with this DA are relatively close to those for the asymptotic DA (the ratio for all π channels lies in the range 1.2 – 1.4). We note that, if a broader pion DA were to be confirmed and quantified, the predicted $\gamma\pi$ photoproduction cross sections would increase accordingly, as discussed above.

Quark and gluon components of η and η' - In describing the $\gamma\eta$ and $\gamma\eta'$ channels, two types of mixing must be taken into account. The phenomenological mixing between the flavour-octet η_8 and flavour-singlet η_1

states is taken into account through (2.37-2.39). The flavour-singlet state η_1 itself contains quark (η_{1q}) and gluon (η_{1g}) components that mix under evolution. Including the gluonic contributions and exploring their impact on the structure of the η and η' mesons was one of the main motivations for this study. Figure 12 displays the fully differential cross-sections for $\gamma\eta$ (thin lines) and $\gamma\eta'$ (thick lines) photoproduction as functions of α , for two choices of renormalization and factorization scales. Predictions that include only quark contributions are shown as dot-dashed lines, while solid lines represent the complete results with gluons included. For the quark-only case, the $\gamma\eta$ cross-sections are higher than those for $\gamma\eta'$, reflecting the relative size of the decay constants. The inclusion of gluons modifies the $\gamma\eta$ results destructively at backward ($\alpha < 0.5$) and constructively at forward ($\alpha > 0.5$) angles. The effect is even stronger for $\gamma\eta'$, where constructive interference lifts the $\gamma\eta'$ predictions above the $\gamma\eta$ ones in the forward region for the default scale choice (4.3), and entirely above for (4.4).

An analogous behaviour is shown in Figures 17 and 18, where the single differential cross-sections are presented for selected values of $S_{\gamma N} = 20$ and 10 GeV^2 and for two choices of the renormalization and factorization scales, μ_R and μ_F . In addition to the quark-only predictions (dot-dashed lines) and the full results including gluons (solid lines), we also display the gluon-only contributions (dotted lines). A comparison of the quark-only and total results shows that for $\gamma\eta$, the gluon effect is relatively small, reducing the prediction at low ξ and increasing it at large ξ . For $\gamma\eta'$, in contrast, the gluon contribution is sizable and increases the result across the entire ξ range. The integrated cross-section shown in Figure 22 confirms the same trend: the gluon effect on $\gamma\eta$ is moderate and reduces the quark-only prediction, while for $\gamma\eta'$ it is large and enhances it. These findings demonstrate that $\gamma\eta'$ photoproduction is highly sensitive to the gluonic component of the η' meson.

Evolution and dependence on factorization scale - In this work, we have examined the impact of the evolution of meson distribution amplitudes and the sensitivity of the predictions to the choice of factorization scale. Two representative choices of μ_F are singled out: (4.3) and (4.4). The effect of DA evolution (B.6) -and consequently the dependence of the leading-order (LO) photoproduction prediction on the μ_F scale¹³ is found to be small for the default pion DA choice (second equation in (4.3)), even when using (4.4). The influence of evolution for the broader DAs is expected to be more pronounced, but including the full evolution requires either an approximation of the infinite Gegenbauer expansion or a numerical solution of the evolution equation. We leave its implementation for future work.

The DA evolution plays a crucial role in the description of η and η' mesons, where it mixes the quark and gluon components of η_1 (B.7), while η_8 obeys the same evolution as pions. Figures 8 and 9, together with the left and right panels of Figure 12, compare the fully differential cross-sections for $\gamma\eta$ and $\gamma\eta'$ photoproduction for renormalization and factorization scales chosen as $\mu_F^2 = s'$ (4.3) and $\mu_F^2 = s'\alpha\bar{\alpha}$ (4.4). The renormalization scale, discussed in Section 4.3, mainly affects the overall normalization, whereas the change in the shape of the predictions, i.e., their dependence on α , originates from the DA evolution to different factorization scales. For $\gamma\eta$, which is mainly governed by the flavour-octet component η_8 , the shape remains almost unchanged, whereas for $\gamma\eta'$ photoproduction, driven by the flavour-singlet component η_1 , the difference becomes clearly visible. In particular, one observes a pronounced backward dominance of the $\gamma\eta'$ predictions at the lower renormalization scale (4.4). This feature is only partly an artefact of the dependence of α_{\max} on the meson mass (3.9), which restricts the available α range in the forward region. A more detailed inspection of individual contributions shows that the gluon terms themselves are backward-dominated, due to the dominant $\mathcal{T}_{\Delta B5}$ contribution listed in Tables 1 and 2 and convoluted by vector GPDs. Consequently, the lower μ_F scale exposes

¹³The hard-scattering subamplitude \mathcal{T} develops an explicit dependence on μ_F only at NLO.

the dominant gluon contributions both in shape and magnitude (as seen from the comparison of the quark-only and total predictions). As expected from the evolution equation, the gluon contributions decrease with increasing scale.

Figures 15 and 16 show that the individual GPD contributions to the single differential cross-sections retain the same shape for $\gamma\eta$ photoproduction for the two scale choices considered, whereas they are significantly modified in the case of $\gamma\eta'$ photoproduction. Figure 17 clearly illustrates that the corresponding curves for $\gamma\eta$ photoproduction (except at very low $S_{\gamma N}$) remain nearly identical when evaluated at different factorization scales. Figure 18, by contrast, shows a distinct change in both the shape and the magnitude of the gluon contributions, which become larger at smaller factorization scales and thereby modify the interplay between the quark and gluon components. Finally, the integrated cross-section shown in Figure 22 exhibits essentially the same pattern: a change in the factorization scale does not affect the shape of the $\gamma\eta$ predictions, whereas for $\gamma\eta'$, the relation between the quark-only and total results differs markedly between scales, once again emphasizing the enhanced role of the gluon contributions at lower scales.

4.3 Normalization and scale dependence

In this work, the amplitudes are calculated at LO in the strong coupling constant. Consequently, the resulting predictions are proportional to $\alpha_s(\mu_R)$ and exhibit a strong dependence on the choice of the renormalization scale. To stabilize this dependence, one must include the NLO corrections,¹⁴ a technically demanding task. Similarly, the dependence on the factorization scale μ_F enters the subprocess amplitudes only at NLO. We have already discussed the dependence of the meson DAs on μ_F and its implications, while the evolution of the GPDs with μ_F is left for a future extension of this work. To illustrate the sensitivity of our predictions to the choice of renormalization scale, we show the results obtained with the default setting $\mu_R^2 = s'$ (4.3) and with $\mu_R^2 = s'\alpha(1 - \alpha)$ (4.4).

The ratio of the fully differential cross-sections obtained with (4.4) and (4.3) follows the expected $\alpha_s^2(s'\alpha\bar{\alpha})/\alpha_s^2(s')$ scaling, which in itself explains most of the observed enhancement by a factor of 2.2–4.5 for pions at $s' = 4 \text{ GeV}^2$ across the allowed α range. Assuming $\mu_R = \mu_F$, the remaining discrepancy arises from the mild factorization-scale dependence discussed above. By comparing Figures 8 and 9, as well as the panels in Figure 12, one finds that the corresponding ratio is about 2 – 3 for η , and increases to 3.6 – 10 for η' . Similarly, the ratios of the single differential cross-sections evaluated at (4.4) and (4.3) are 2.5 – 3 for π^\pm and 2.5 – 3.5 for π^0 . The single differential cross-sections shown in Figs. 15–18 indicate ratios of 2.2 – 2.7 for η and 4 – 6.5 for η' . Finally, the integrated cross-sections presented in Figures 20 and 22 yield approximately constant ratios across the relevant $S_{\gamma N}$ range: 2.6 – 2.7 for pions, 2.1 – 2.5 for η , and 5.1 – 5.2 for η' . The systematically larger enhancement observed for η' across all considered observables arises from the factorization-scale dependence of the gluon contributions and their interference with the quark contributions.

Figures 20 and 22 show that the integrated cross-sections, obtained for our chosen set of parameters, DAs, and GPDs, reach values of a few tens of pb. These absolute values should not be interpreted too strictly, as our approach is applicable only at moderate ξ and does not include the contributions relevant at small ξ , such as those from sea quarks and gluons in the nucleon. Since the subprocess amplitudes, GPDs, and DAs are identical, the observed ordering of the pion cross-sections, $\sigma_{\pi^-} > \sigma_{\pi^+} > \sigma_{\pi^0}$, is entirely determined by the meson flavour structure, i.e. the charge factors. The cross-sections for η and η' are somewhat smaller, with $\sigma_\eta > \sigma_{\eta'}$ for the default scale choice (4.3), whereas for (4.4) the

¹⁴NLO corrections contain both constant and $\log(\mu_R)$ -dependent terms, which reduce the sensitivity to μ_R .

η' cross-section exceeds that of η at higher values of $S_{\gamma N}$. Similarly, App. E.2 shows that the single differential cross-sections $d\sigma/d\xi$ for $\xi > 0.1$ reach values of a few hundred pb, while the fully differential cross-sections presented in App. E.1 are of the order of a few tens of pb GeV⁻⁴. Both vary strongly depending on the specific kinematical conditions.

4.4 Numerical summary

We have carried out a detailed analysis of the fully differential, single differential and integrated cross-sections for γM photoproduction, valid in the moderate- ξ region ($\xi > 0.1$). We want to stress the following findings regarding the key aspects of this analysis stated at the beginning of this section:

- Our results show that in the moderate- ξ region the pion-pole term $\tilde{\mathcal{E}}_{\text{pole}}$ plays a particularly significant role, most notably in $\gamma\pi^\pm$ photoproduction, where its contribution becomes especially pronounced at backward scattering angles. Pion-pole effects are also present in the photoproduction of neutral mesons. Apart from the pion-pole term, the vector GPD contributions, in particular \mathcal{H} , dominate the observable. See, e.g., Fig.5.
- Photoproduction of $\gamma\pi$ pairs is particularly sensitive to the shape of the pion DAs, and in the moderate- ξ region this sensitivity is further enhanced by the pion-pole contributions (2.43). The results obtained with the default moment-based lattice DA $\phi_{[0.116]}$ (2.34) are close to those obtained with the commonly used asymptotic DA, whereas the predictions obtained with the broader DAs (2.35) can be significantly larger. For the fully differential cross section, the average ratio of the predictions obtained with the broad DA $\phi_\pi^{(0.3)}$ and the asymptotic DA is about 5.5 for π^+ , 4.5 for π^- , and 3 for π^0 . See, e.g., Fig.11.
- The study of $\gamma\eta$ and $\gamma\eta'$ channels provides valuable insight into the gluon content of these mesons. In particular, the $\gamma\eta'$ channel shows sizeable gluon contributions in η' meson and a strong sensitivity to the factorization-scale choice. See, e.g., Fig.12.
- The variation of the LO predictions with the renormalization scale introduces potentially large theoretical uncertainties, highlighting the importance of NLO corrections. We have compared the results at two physically motivated large-scale choices for the renormalization scale: the γM invariant mass (4.3) and the square of relative momentum transfer between the photon and meson (4.4). For our kinematic settings, the corresponding predictions exhibit a sizeable μ_R dependence, with the latter choice producing an enhancement of about 2–4 times. In the η' channel, the strong dependence on the factorization scale amplifies this effect. See, e.g., Figs. 18 and 20.

5 Conclusions

In this work, we revisit the hard exclusive photoproduction of photon–meson pairs, $\gamma N \rightarrow \gamma M N'$, and evaluate the corresponding cross sections at leading twist and leading order in perturbative QCD. The core of the analytical calculation, summarized in Section 2.4, consists of compact expressions for the subprocess amplitudes in the pseudoscalar channels $M \in \{\pi^\pm, \pi^0, \eta, \eta'\}$, including only the quark GPD contributions while also taking into account the two–gluon components of the η and η' distribution amplitudes. These results provide a transparent structure of the amplitudes and a practical basis for efficient numerical implementation.

The phenomenological analysis is performed in the moderate- ξ region ($\xi > 0.1$), with the adopted valence–quark approximation, in which the valence contributions are numerically sizable, while the sea–quark and gluon contributions are consistently omitted. The latter would require a modified

factorisation framework for their reliable inclusion. The pion–pole contribution plays a central role in this kinematic domain. It provides the main contribution in $\gamma\pi^\pm$ production and has a visible impact in the neutral channels as well. Including the pion–pole term is therefore essential in the moderate– ξ region relevant for JLab and COMPASS/AMBER measurements [22, 63], whereas for small ξ , its effect becomes negligible. All leading–twist chiral–even GPDs are included in our analysis, and the vector contributions, in particular \mathcal{H} , generally dominate once the pion–pole term is absent.

Our analysis shows a strong sensitivity of $\gamma\pi$ production to the shape of the pion distribution amplitude, with broad DAs possibly enhancing the predictions several times in comparison with the asymptotic DA. The $\gamma\eta$ and $\gamma\eta'$ channels probe the gluon content of the mesons, with gluons contributing already at LO in this process. This is in contrast to the $\gamma^*\gamma \rightarrow \eta(\eta')$ transition form factors, which are used to constrain the meson DAs from experiment, where gluon contributions appear only at NLO. Interestingly, in deeply virtual production of η and η' mesons, the two–gluon contributions vanish at LO for kinematic reasons [64]. The presence of gluon contributions already at LO therefore makes photon-meson photoproduction particularly suited for studying the gluonic components of the η and η' mesons. In this case, the $\gamma\eta'$ channel shows sizeable two–gluon contributions and a strong dependence on the factorization scale.

Being a LO QCD prediction, the numerical results are strongly dependent on the choice of the renormalization scale, indicating that the inclusion of NLO corrections is essential for stabilizing this dependence and achieving a quantitatively reliable description. At the subprocess level, photon-meson photoproduction is closely related to wide-angle meson-pair production, $\gamma\gamma \rightarrow MM'$, and valuable insights can be gained by comparing the two processes. In particular, the pseudoscalar-pseudoscalar (PP) channel has been analyzed at NLO [56], and extending this analysis, involving a few hundred diagrams, to photoproduction kinematics as well as to the scalar-pseudoscalar (SP) channel remains an ambitious task. Nevertheless, taking lessons from DVCS and DVMP, for which a consistent description based on universal GPDs emerges only at NLO [7], we view this as a well-motivated and natural extension. In the absence of NLO corrections, we therefore compare our predictions at two physically motivated scale choices and find markedly different results, differing by a factor of a few.

The present study establishes a consistent and transparent leading-order framework for photon–meson photoproduction, with the quark GPD contributions included. This process is complementary to DVCS and DVMP in providing information on GPDs, but is more sensitive to their x -dependence due to the additional kinematic variables and the mixing of x with external scales in the propagators [10]. The analytical and numerical results presented here provide a reference baseline for forthcoming experimental studies at JLab, COMPASS/AMBER, and future facilities, which will ultimately enable a more precise determination of GPDs and improve our understanding of nucleon structure.

Acknowledgments

We thank P. Kroll, Pawel Nadel-Turonski and Justin Stevens for discussions. This publication was partially supported by the Croatian Science Foundation project IP-2019-04-9709 and N. Crnković was supported by the Croatian Science Foundation project DOK-2020-01-9883. L. Szymanowski was supported by the Grant No. 2024/53/B/ST2/00968 of the National Science Centre in Poland. He thanks IJCLab and the "P2I - Graduate School of Physics", in the framework "Investissements d'Avenir" (ANR-11-IDEX-0003-01) managed by the Agence Nationale de la Recherche (ANR), France, for support. The work of S. N. was supported by the Science and Technology Facilities Council (STFC) under Grant No. ST/X00077X/1, and by the Royal Society through Grant No. URF/R1/201500.

A Kinematics

We choose the light-cone vectors p and n as

$$p^\mu = \frac{\sqrt{s_0}}{2}(1, 0, 0, 1), \quad n^\mu = \frac{\sqrt{s_0}}{2}(1, 0, 0, -1), \quad (\text{A.1})$$

which satisfy $p^2 = n^2 = 0$ and $p \cdot n = s_0/2$, while s_0 is the auxiliary scale. A generic four-momentum v^μ can then be decomposed in the Sudakov basis as

$$v^\mu = a n^\mu + b p^\mu + v_\perp^\mu, \quad \text{with} \quad v_\perp^\mu = (0, v^x, v^y, 0), \quad (\text{A.2})$$

so that $v^2 = a b s_0 + v_\perp^2$.

With this convention, and adopting the usual definition $\Delta = p_2 - p_1$ given in Eq. (2.4), the particle momenta for the process (2.1) can be expressed as

$$\begin{aligned} p_1^\mu &= (1 + \xi) p^\mu + \frac{m_N^2}{s_0(1 + \xi)} n^\mu, & p_2^\mu &= (1 - \xi) p^\mu + \frac{m_{N'}^2 - \Delta_\perp^2}{s_0(1 - \xi)} n^\mu + \Delta_\perp^\mu, \\ q^\mu &= n^\mu, & k^\mu &= \alpha n^\mu - \frac{(\kappa_\perp - \Delta_\perp/2)^2}{s_0 \alpha} p^\mu + \kappa_\perp^\mu - \frac{\Delta_\perp^\mu}{2}, \\ p_M^\mu &= \alpha_M n^\mu + \frac{-(\kappa_\perp + \Delta_\perp/2)^2 + m_M^2}{s_0 \alpha_M} p^\mu - \kappa_\perp^\mu - \frac{\Delta_\perp^\mu}{2}. \end{aligned} \quad (\text{A.3})$$

Here, $m_N \approx m_{N'}$ and m_M denote the nucleon and meson masses, respectively, while κ_\perp represents the relative transverse momentum between the outgoing photon and the meson. We introduce the dimensionless variables α , α_M , and ξ . The latter, as usual, denotes the skewness (2.5).

From (A.3) follows that scalars (2.2) amount to

$$\begin{aligned} S_{\gamma N} &= (1 + \xi) s_0 + m_N^2, & t &= \Delta^2 = -\frac{4\xi^2 m_N^2}{1 - \xi^2} + \frac{1 + \xi}{1 - \xi} \Delta_\perp^2, \\ s' &= M_{\gamma M}^2 = 2\xi s_0 + t, & t' &= \frac{(\kappa_\perp - \Delta_\perp/2)^2}{\alpha}, & u' &= \frac{(\kappa_\perp + \Delta_\perp/2)^2 - (1 - \alpha_M) m_M^2}{\alpha_M}, \end{aligned} \quad (\text{A.4})$$

while a similar lengthy expression for $M_{MN'}^2$ can be found in [8, 9]. Skewness then takes the general form

$$\xi = \frac{\tau}{2 - \tau} \quad \text{with} \quad \tau = \frac{s' - t}{S_{\gamma N} - m_N^2}. \quad (\text{A.5})$$

According to factorization, illustrated in Fig. 1, κ_\perp needs to be large, implying large $s' = M_{\gamma M}^2$ and t' and one neglects Δ_\perp in front of κ_\perp . In the collinear approximation, or so-called generalized Bjorken limit, needed for the determination of subprocess amplitudes (2.7, 2.8), one also neglects the hadronic masses. Thus

$$s' = M_{\gamma M}^2 \approx -\frac{\kappa_\perp^2}{\alpha \bar{\alpha}} = 2\xi s_0, \quad -t' \approx -\frac{\kappa_\perp^2}{\alpha} = \bar{\alpha} s', \quad -u' \approx -\frac{\kappa_\perp^2}{\bar{\alpha}} = \alpha s', \quad (\text{A.6})$$

with $\alpha_M \approx 1 - \alpha \equiv \bar{\alpha}$, while $t = 0$.

B Distribution amplitude formalism: convention and evolution

The definition (2.28) of meson DAs describes the projection of a collinear $q\bar{q}$ state onto a pseudoscalar meson M . It is applied to evaluation of Feynman diagrams, as in Fig. 3, by replacing the quark and antiquark spinors¹⁵ with the projector

$$\mathcal{P}_{M,q}^{ij,kl} = C_M^{ij} \frac{\delta_{kl}}{4N_c} \gamma_5 \not{p}_M, \quad (\text{B.1})$$

where (i, k) and (j, l) denote the (flavour, colour) indices of the quark and antiquark, respectively. For the diagrams in Fig. 4, a collinear gg state of two outgoing gluons¹⁶ with colour indices a and b , Lorentz indices μ and ν , and momentum fractions z and \bar{z} , is projected onto the flavour-singlet pseudoscalar state η_1 as

$$\mathcal{P}_{\eta_1,g}^{\mu\nu,ab} = \frac{1}{2\sqrt{n_f}} \frac{\delta_{ab}}{4N_c} i \varepsilon_{\perp}^{\mu\nu} \frac{1}{z\bar{z}}, \quad \varepsilon_{\perp}^{\mu\nu} = \varepsilon_{\gamma\delta}^{\mu\nu} \frac{k^\gamma p_M^\delta}{k \cdot p_M}, \quad (\text{B.2})$$

with k here satisfying the standard light-cone requirements, being collinear to p_M in the light-cone sense (non-zero minus and vanishing transverse components), so that it serves as the reference vector in the projection. The factor $1/(z\bar{z})$ arises from converting the field-strength tensor matrix element (2.30) to the gauge-field representation $\langle \eta_1(p_M) | A^\nu(-w) A^\mu(w) | 0 \rangle$, which appears in the amplitude evaluation. Throughout this work for the Levi-Civita tensor we adopt the convention

$$\epsilon^{0123} = +1. \quad (\text{B.3})$$

The projectors (B.1) and (B.2) are then used in the calculation of the hard-scattering subprocess amplitudes, which are subsequently convoluted with $f_M \phi_M$ and $f_{\eta_1} \phi_{\eta_1,g}$, respectively.

For completeness, we note that in the case of scalar mesons, the definitions are modified as follows: γ_5 is omitted in (2.28) and (B.1); the dual field-strength tensor is replaced by $\tilde{G}^{\mu\nu} \rightarrow G^{\mu\nu}$, and $i \varepsilon_{\perp}^{\mu\nu} \rightarrow g_{\perp}^{\mu\nu} = g^{\mu\nu} - \frac{k^\mu p^\nu + k^\nu p^\mu}{k \cdot p_M}$ in (2.30) and (B.2), respectively. The symmetry properties given in (2.31) change sign for scalar mesons.

The definition of the gluon DA and the corresponding flavor-singlet evolution is convention dependent¹⁷. In this work we adopt the convention of Ref. [42], developed and employed in Refs. [40, 41, 43]. For completeness, we summarize the LO evolution equations for quark and gluon DAs of pseudoscalar mesons represented as Gegenbauer expansions:

$$\phi_M(z; \mu_F) = 6z(1-z) \left(1 + \sum_{n=2,4,\dots} a_n^M(\mu_F) C_n^{3/2}(2z-1) \right), \quad (\text{B.4})$$

$$\phi_{\eta_1,g}(z; \mu_F) = 30z^2(1-z)^2 \sum_{n=2,4,\dots} a_n^g(\mu_F) C_{n-1}^{5/2}(2z-1), \quad (\text{B.5})$$

¹⁵Spinors are normalized as $u^\dagger(p, \lambda) u(p, \lambda') = \sqrt{2} p^+ \delta_{\lambda\lambda'}$.

¹⁶The complex-conjugated expression applies for an incoming pseudoscalar meson.

¹⁷A detailed discussion of the various conventions found in the literature is provided in Ref. [40]. The evolution kernels corresponding to the present convention were summarized in Ref. [41], where η and η' transition form factors were also employed to update the numerical values of the DA coefficients. The same formalism and DAs were later applied to other processes in Refs. [42, 43], where a slightly modified normalization-affecting the DA coefficients -was introduced for convenience.

where the flavour-octet pseudoscalar mesons $M = \{\pi^+, \pi^-, \pi^0, \eta_8\}$ evolve according to

$$a_n^M(\mu_F) = a_n^M(\mu_0) L^{\gamma_n^{qq}/\beta_0}, \quad L = \frac{\alpha_s(\mu_0)}{\alpha_s(\mu_F)}. \quad (\text{B.6})$$

For the flavour-singlet η_1 , the evolution mixes the quark $\phi_{\eta_{1q}} \equiv \phi_{\eta_1}$ and gluon DAs $\phi_{\eta_{1g}}$:

$$\begin{aligned} a_n^1(\mu_F) &= \frac{1}{1 - \rho_n^{(+)} \rho_n^{(-)}} \left[(L^{\gamma_n^{(+)} / \beta_0} - \rho_n^{(+)} \rho_n^{(-)} L^{\gamma_n^{(-)} / \beta_0}) a_n^1(\mu_0^2) + (L^{\gamma_n^{(-)} / \beta_0} - L^{\gamma_n^{(+)} / \beta_0}) \rho_n^{(-)} a_n^g(\mu_0^2) \right], \\ a_n^g(\mu_F) &= \frac{1}{1 - \rho_n^{(+)} \rho_n^{(-)}} \left[(L^{\gamma_n^{(-)} / \beta_0} - \rho_n^{(+)} \rho_n^{(-)} L^{\gamma_n^{(+)} / \beta_0}) a_n^g(\mu_0^2) + (L^{\gamma_n^{(+)} / \beta_0} - L^{\gamma_n^{(-)} / \beta_0}) \rho_n^{(+)} a_n^1(\mu_0^2) \right], \end{aligned} \quad (\text{B.7})$$

with

$$\rho_n^{(+)} = \frac{1}{5} \frac{\gamma_n^{gq}}{\gamma_n^{(+)} - \gamma_n^{gg}}, \quad \rho_n^{(-)} = 5 \frac{\gamma_n^{gg}}{\gamma_n^{(-)} - \gamma_n^{qq}}, \quad (\text{B.8})$$

and eigenvalues of the anomalous-dimension matrix

$$\gamma_n^{(\pm)} = \frac{1}{2} \left[\gamma_n^{qq} + \gamma_n^{gg} \pm \sqrt{(\gamma_n^{qq} - \gamma_n^{gg})^2 + 4 \gamma_n^{gq} \gamma_n^{gq}} \right]. \quad (\text{B.9})$$

The LO anomalous dimensions used in this convention read

$$\begin{aligned} \gamma_n^{qq} &= C_F \left[3 + \frac{2}{(n+1)(n+2)} - 4 \sum_{i=1}^{n+1} \frac{1}{i} \right], & \gamma_n^{gq} &= C_F \frac{n(n+3)}{3(n+1)(n+2)}, \quad n \geq 2, \\ \gamma_n^{gq} &= n_f \frac{12}{(n+1)(n+2)}, \quad n \geq 2, & \gamma_n^{gg} &= \beta_0 + N_c \left[\frac{8}{(n+1)(n+2)} - 4 \sum_{i=1}^{n+1} \frac{1}{i} \right], \quad n \geq 2. \end{aligned} \quad (\text{B.10})$$

where $C_F = (N_c^2 - 1)/(2N_c)$ and $\beta_0 = (11/3)N_c - (2/3)n_f$. One should distinguish between $n_f = 3$, used in (B.10) and in the DA definitions (2.28) and (2.30), which counts the fixed valence-quark content in the meson's flavor-singlet combination, and \tilde{n}_f , the number of active flavors at a given scale, which enters the β functions and governs the running of α_s .

C Hard-scattering amplitudes for mesons with non-symmetric DAs

For completeness, this section provides the hard-scattering amplitudes for the $\gamma q_i \rightarrow (q_i \bar{q}_j) q_j$ (or equivalently, $\gamma(q_i \bar{q}_j) \rightarrow (q_i \bar{q}_j)$) subprocess, without taking into account the symmetry properties of the meson DA. Unlike the symmetrized expressions in Sec. 2.4, these results apply to pseudoscalar mesons with non-symmetric DAs, such as kaons. The full hard-scattering amplitude for the $\gamma(P) \rightarrow \gamma P$ subprocess, which couples to the parity-odd (axial) GPD, reads

$$\mathcal{T}_{\text{PP}}^{(ij)} = \left(e_i^2 \mathcal{T}_A^{(i)} + e_j^2 \mathcal{T}_A^{(j)} + e_i e_j \mathcal{T}_A^{(ij)} \right) T_A + \left(e_i^2 \mathcal{T}_B^{(i)} + e_j^2 \mathcal{T}_B^{(j)} + e_i e_j \mathcal{T}_B^{(ij)} \right) T_B, \quad (\text{C.1})$$

where

$$\begin{aligned} \mathcal{T}_A^{(i)}(y, z) &= \frac{4}{s' \bar{\alpha}} \left(\frac{\alpha - z}{z \bar{z} (y + i\epsilon)} + \frac{1 - \alpha z}{\alpha z \bar{z} (y - i\epsilon)} + \frac{\bar{\alpha}^2 - 2\alpha z}{\alpha z \bar{z} (\bar{y} - i\epsilon)} \right), \\ \mathcal{T}_A^{(ij)}(y, z) &= \frac{4}{s' \alpha} \left(\frac{\alpha - z}{z \bar{z} (y + i\epsilon)} - \frac{1 - \alpha \bar{z}}{z \bar{z} (\bar{y} - i\epsilon)} - \frac{(1 - \bar{\alpha} z)^2 + \alpha}{z \bar{z} (\bar{z} y - \alpha z \bar{y} + i\epsilon)} \right) + \left\{ (y, z) \rightarrow (\bar{y}, \bar{z}) \right\}, \end{aligned} \quad (\text{C.2})$$

$$\begin{aligned} \mathcal{T}_B^{(i)}(y, z) &= \frac{8}{s'^2 \alpha} \left(-\frac{1}{\bar{\alpha} \bar{z} (y + i\epsilon)} + \frac{1}{\alpha \bar{\alpha} \bar{z} (y - i\epsilon)} + \frac{1}{\alpha z (\bar{y} - i\epsilon)} \right), \\ \mathcal{T}_B^{(ij)}(y, z) &= \frac{8}{s'^2 \alpha^2} \left(-\frac{1}{\bar{z} (y + i\epsilon)} - \frac{1}{z (\bar{y} - i\epsilon)} \right) + \left\{ (y, z) \rightarrow (\bar{y}, \bar{z}) \right\}, \end{aligned} \quad (\text{C.3})$$

while

$$\mathcal{T}_A^{(j)}(y, z) = \mathcal{T}_A^{(i)}(\bar{y}, \bar{z}), \quad \mathcal{T}_B^{(j)}(y, z) = \mathcal{T}_B^{(i)}(\bar{y}, \bar{z}). \quad (\text{C.4})$$

The amplitude for the $\gamma(S) \rightarrow \gamma P$ subprocess couples to the parity-even (vector) GPD and is given by

$$\mathcal{T}_{\text{SP}}^{(ij)} = \left(e_i^2 \mathcal{T}_{A5}^{(i)} + e_j^2 \mathcal{T}_{A5}^{(j)} + e_i e_j \mathcal{T}_{A5}^{(ij)} \right) T_{A5} + \left(e_i^2 \mathcal{T}_{B5}^{(i)} + e_j^2 \mathcal{T}_{B5}^{(j)} + e_i e_j \mathcal{T}_{B5}^{(ij)} \right) T_{B5}, \quad (\text{C.5})$$

with

$$\begin{aligned} \mathcal{T}_{A5}^{(i)}(y, z) &= \frac{-16\xi i}{s'^3 \alpha \bar{\alpha}} \left(\frac{\alpha(z - \bar{z}) - z}{\bar{\alpha} z \bar{z} (y + i\epsilon)} + \frac{1 - \alpha z}{\alpha \bar{\alpha} z \bar{z} (y - i\epsilon)} - \frac{1 + \alpha(z - \bar{z})}{\alpha z \bar{z} (\bar{y} - i\epsilon)} \right), \\ \mathcal{T}_{A5}^{(ij)}(y, z) &= \frac{-16\xi i}{s'^3 \alpha^2} \left(\frac{\alpha(z - \bar{z}) - z}{\bar{\alpha} z \bar{z} (y + i\epsilon)} + \frac{1 - \alpha \bar{z}}{\bar{\alpha} z \bar{z} (\bar{y} - i\epsilon)} + \frac{\alpha z^2 - \bar{z}^2}{z \bar{z} (\bar{z} y - \alpha z \bar{y} + i\epsilon)} \right) - \left\{ (y, z) \rightarrow (\bar{y}, \bar{z}) \right\}, \end{aligned} \quad (\text{C.6})$$

$$\begin{aligned} \mathcal{T}_{B5}^{(i)}(y, z) &= \frac{-16\xi i}{s'^3 \alpha \bar{\alpha}} \left(\frac{\alpha - z}{\bar{\alpha} z \bar{z} (y + i\epsilon)} + \frac{z - \bar{z} - \alpha z}{\alpha \bar{\alpha} z \bar{z} (y - i\epsilon)} - \frac{\bar{\alpha} - 2z}{\alpha z \bar{z} (\bar{y} - i\epsilon)} \right), \\ \mathcal{T}_{B5}^{(ij)}(y, z) &= -\mathcal{T}_{A5}^{(ij)}(y, z) + \frac{32\xi i}{s'^3 \alpha^2} \left(\frac{1}{\bar{z} (y + i\epsilon)} - \frac{1}{z (\bar{y} - i\epsilon)} - \left\{ (y, z) \rightarrow (\bar{y}, \bar{z}) \right\} \right) \\ &= -\mathcal{T}_{A5}^{(ij)}(y, z) + \mathcal{T}_{\Delta B5}^{(ij)}(y, z), \end{aligned} \quad (\text{C.7})$$

while

$$\mathcal{T}_{A5}^{(j)}(y, z) = -\mathcal{T}_{A5}^{(i)}(\bar{y}, \bar{z}), \quad \mathcal{T}_{B5}^{(j)}(y, z) = -\mathcal{T}_{B5}^{(i)}(\bar{y}, \bar{z}). \quad (\text{C.8})$$

D Calculation of PV integrals

Here, as defined in (2.11), we adopt the compact notation $y = \frac{\xi+x}{2\xi}$, $\bar{y} = \frac{\xi-x}{2\xi}$, and use $\otimes \equiv \otimes^x = \otimes^y$ and $\overset{z}{\otimes}$ to denote the convolution integrals defined in (2.23). We explain here the PV treatment of the elementary contributions (2.55).

Using the standard distribution identity

$$\frac{1}{y \pm i\epsilon} = \mathcal{P} \frac{1}{y} \mp i\pi \delta(y), \quad (\text{D.1})$$

the convolution with a GPD yields

$$\mathcal{P} \frac{1}{y} \otimes H(x, \xi) = \int_{-1}^1 dx \frac{1}{\xi+x} [H(x, \xi) - H(-\xi, \xi)] + \ln \frac{1+\xi}{1-\xi} H(-\xi, \xi), \quad (\text{D.2})$$

$$\delta(y) \otimes H(x, \xi) = H(-\xi, \xi). \quad (\text{D.3})$$

For mixed denominators of the form $\bar{z}y - \alpha z \bar{y}$, with $\alpha, z \in [0, 1]$, we rewrite the propagator in a form suitable for PV decomposition and using (D.1) get

$$\frac{1}{\bar{z}y - \alpha z \bar{y} + i\epsilon} \rightarrow \frac{-1}{y + \alpha \bar{y}} \left(\mathcal{P} \frac{1}{z - \frac{y}{y + \alpha \bar{y}}} + i\pi \delta \left(z - \frac{y}{y + \alpha \bar{y}} \right) \right). \quad (\text{D.4})$$

The PV contribution in this case leads to a combined convolution over x and z , naturally split into the DGLAP and ERBL regions:

$$\begin{aligned} & \phi(z) \overset{z}{\otimes} f(y, z) \mathcal{P} \frac{1}{z - \frac{y}{y + \alpha \bar{y}}} \otimes H(x, \xi) \\ &= \left[\int_{-1}^{-\xi} + \int_{\xi}^1 \right] \frac{dx}{2\xi} H(x, \xi) \int_0^1 dz \phi(z) f(y, z) \frac{1}{z - \frac{y}{y + \alpha \bar{y}}} \\ &+ \int_{-\xi}^{\xi} \frac{dx}{2\xi} H(x, \xi) \int_0^1 dz \left[\phi(z) f(y, z) - \phi \left(\frac{y}{y + \alpha \bar{y}} \right) f \left(y, \frac{y}{y + \alpha \bar{y}} \right) \right] \frac{1}{z - \frac{y}{y + \alpha \bar{y}}} \\ &- \int_{-\xi}^{\xi} \frac{dx}{2\xi} H(x, \xi) \ln \frac{y}{\alpha \bar{y}} \phi \left(\frac{y}{y + \alpha \bar{y}} \right) f \left(y, \frac{y}{y + \alpha \bar{y}} \right), \end{aligned} \quad (\text{D.5})$$

while the imaginary part resides in ERBL region

$$\phi(z) \overset{z}{\otimes} f(y, z) \delta \left(z - \frac{y}{y + \alpha \bar{y}} \right) \otimes H(x, \xi) = \int_{-\xi}^{\xi} \frac{dx}{2\xi} H(x, \xi) \phi \left(\frac{y}{y + \alpha \bar{y}} \right) f \left(y, \frac{y}{y + \alpha \bar{y}} \right). \quad (\text{D.6})$$

In order to keep the expressions above as compact as possible, we use both y and x notation whenever convenient¹⁸ interchangeably.

¹⁸Note that from $x = \xi(2y - 1)$ follows $\int_{-\xi}^{\xi} \frac{dx}{2\xi} = \int_0^1 dy$, and it is easy to see from (D.4) that the LO contribution to the s-channel process $\gamma M_1 \rightarrow \gamma M_2$ ($0 < y < 1$) develops an imaginary part. In contrast, for the corresponding t-channel process $\gamma\gamma \rightarrow M_1 M_2$, the LO contribution is real within the physical region, while imaginary parts arise only for values of y outside $[0, 1]$ (i.e., $y < 0$ or $y > 1$), as in the subprocess of $\pi N \rightarrow \gamma\gamma N'$. This parallels the observations given in [10, 21], namely the enhanced GPD sensitivity in the ERBL region for $\gamma N \rightarrow \gamma M N'$, and in the DGLAP region for $\pi N \rightarrow \gamma\gamma N'$.

E Compendium of numerical results

In this section, we collect the figures showing the numerical results discussed in Section 4.

E.1 Fully differential cross-section

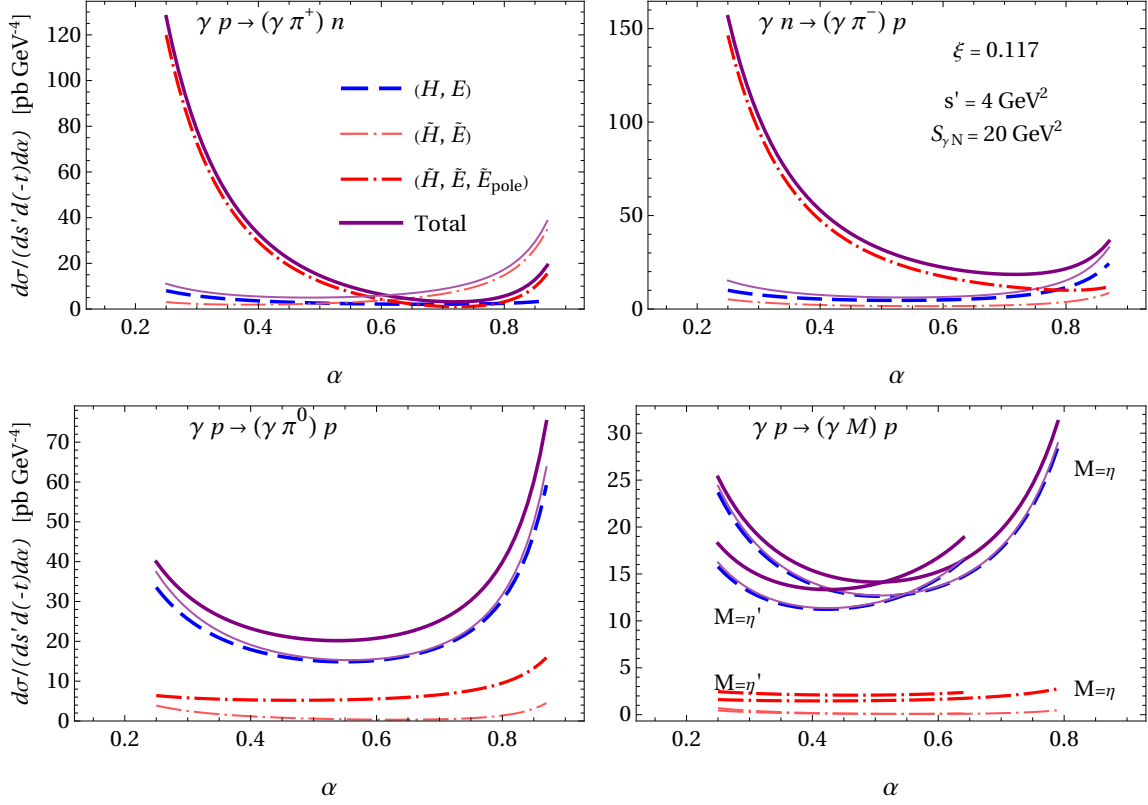


Figure 5: Fully differential cross-section for $\gamma N \rightarrow \gamma M N'$, with $M = \pi^+, \pi^-, \pi^0, \eta, \eta'$. Dashed and dash-dotted lines correspond to the vector and axial-vector GPD contributions, respectively, while solid lines show their sum, i.e., the total result. Thin lines represent axial and total results without the π -pole contribution. The kinematics are specified by $S_{\gamma N} = 20 \text{ GeV}^2$, $s' = 4 \text{ GeV}^2$, yielding $\xi = 0.117$, while $(-t) = (-t_0)$ (3.6).

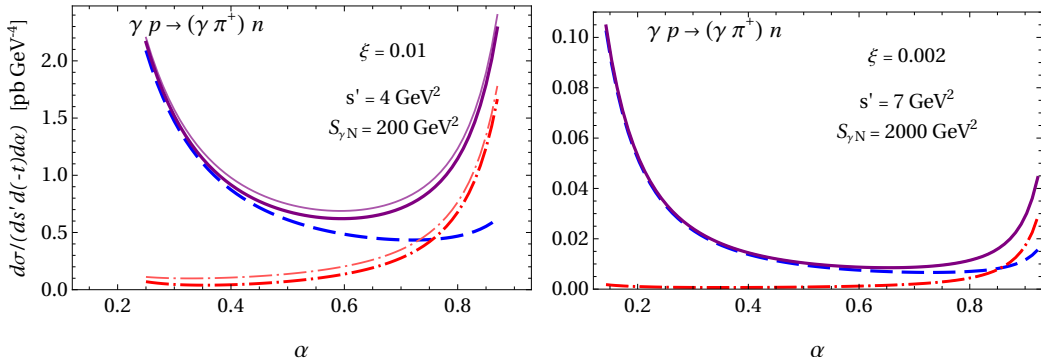


Figure 6: Illustration of the size of the pion-pole contribution to fully differential cross-section for $\gamma p \rightarrow \gamma \pi^+ n$ at small ξ values. Line designations as in Fig. 5, and $(-t) = (-t_0)$.

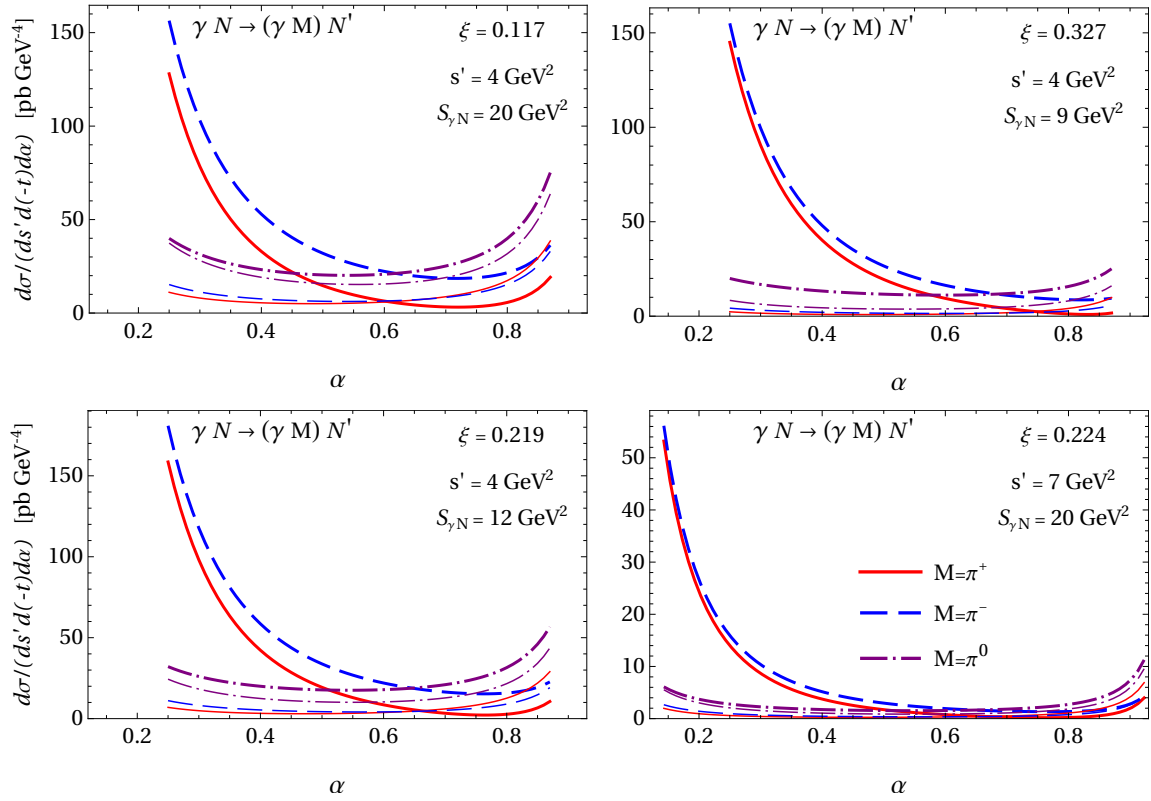


Figure 7: Fully differential cross-section for $\gamma N \rightarrow \gamma \pi N'$ at $(-t) = (-t_0)$ and four different kinematics: ($s' = 4$, $S_{\gamma N} = 20$) GeV^2 with $\xi = 0.117$; ($s' = 4$, $S_{\gamma N} = 12$) GeV^2 with $\xi = 0.219$; ($s' = 7$, $S_{\gamma N} = 20$) GeV^2 with $\xi = 0.224$; and ($s' = 4$, $S_{\gamma N} = 9$) GeV^2 with $\xi = 0.327$. Here π^+ , π^- , and π^0 are represented by solid, dashed, and dot-dashed lines, respectively. Thin lines denote results obtained without the π -pole contribution.

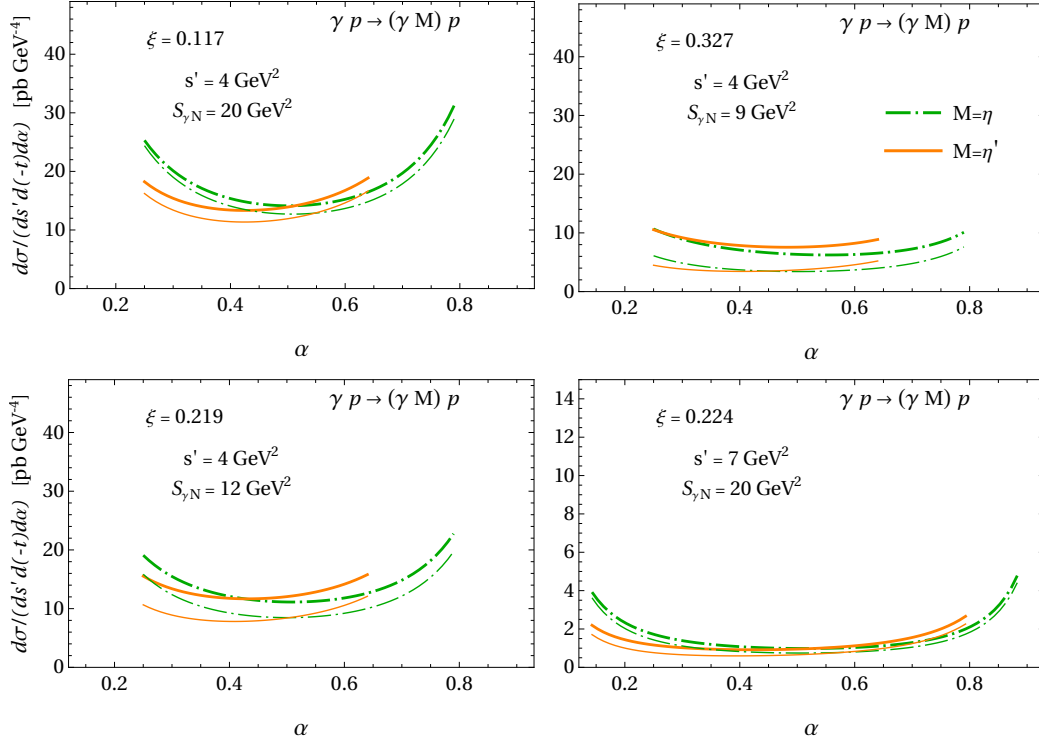


Figure 8: Fully differential cross-section for $\gamma p \rightarrow \gamma\eta(\eta')p$ at $(-t) = (-t_0)$ and four different kinematics: ($s' = 4$, $S_{\gamma N} = 20$) GeV^2 with $\xi = 0.117$; ($s' = 4$, $S_{\gamma N} = 12$) GeV^2 with $\xi = 0.219$; ($s' = 7$, $S_{\gamma N} = 20$) GeV^2 with $\xi = 0.224$; and ($s' = 4$, $S_{\gamma N} = 9$) GeV^2 with $\xi = 0.327$. Here η , and η' are represented by dot-dashed, and solid lines, respectively. Thin lines denote results obtained without the π -pole contribution. The scales are set to $\mu_R^2 = \mu_F^2 = s'$.

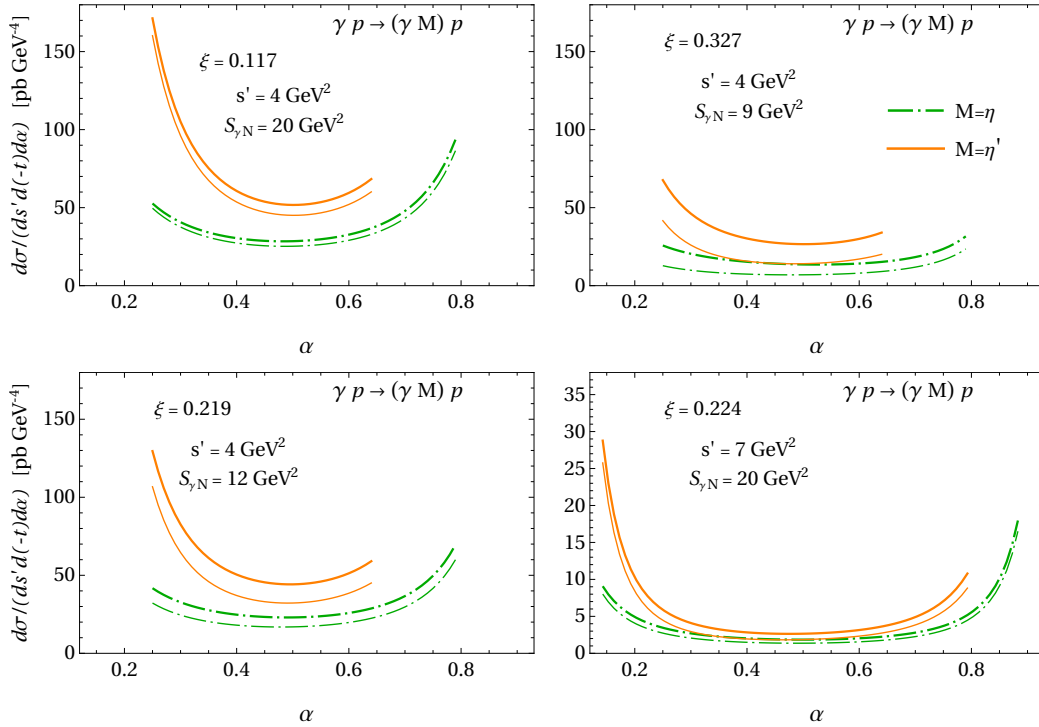


Figure 9: Fully differential cross-section $\gamma p \rightarrow \gamma\eta(\eta')p$ at $(-t) = (-t_0)$ and four different kinematics. Line designations as in Fig. 8. Here the scales are set to $\mu_R^2 = \mu_F^2 = s'\alpha(1 - \alpha)$.

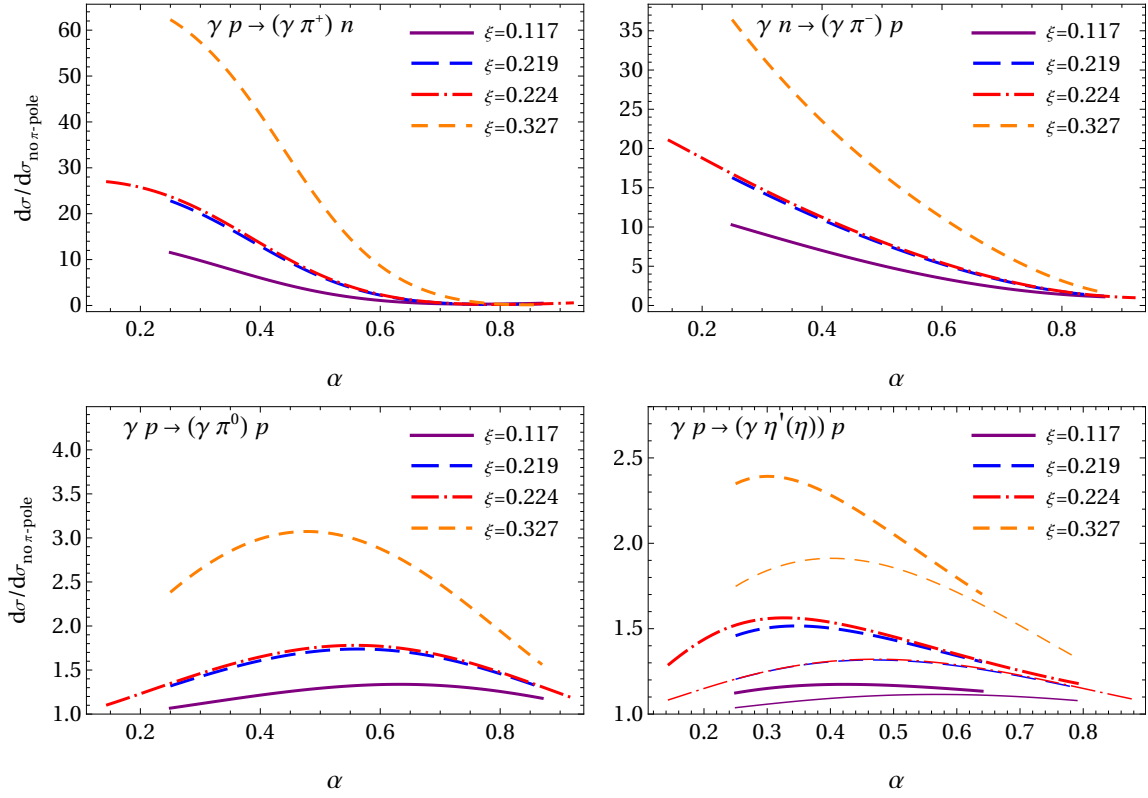


Figure 10: Ratio of the fully differential cross-section (3.1) for the process $\gamma N \rightarrow \gamma M N'$ ($M = \pi^+, \pi^-, \pi^0, \eta, \eta'$) obtained with and without the π -pole contribution. Different kinematics are compared, specified by $\xi = 0.117, 0.219, 0.224,$ and 0.327 , while $(-t) = (-t_0)$. Thin lines in the bottom-right panel correspond to η , while thick lines represent the η' results.

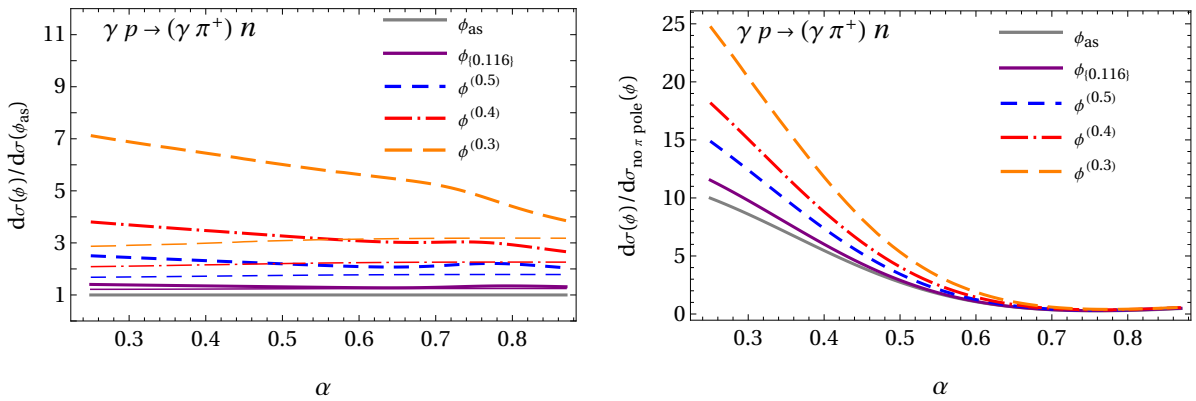


Figure 11: Left: Ratio of the fully differential cross-section (3.1) for $\gamma p \rightarrow \gamma \pi^+ n$, obtained with a given pion DA and normalized to the result with the asymptotic DA. Thick and thin lines denote results with and without the π -pole contribution, respectively. Right: Ratio of the full differential cross-section for the same process, comparing different pion DAs, obtained with and without the π -pole contribution. Both figures are evaluated at $s' = 4 \text{ GeV}^2$ and $S_{\gamma N} = 20 \text{ GeV}^2$, yielding $\xi = 0.117$, and at $(-t) = (-t_0)$.

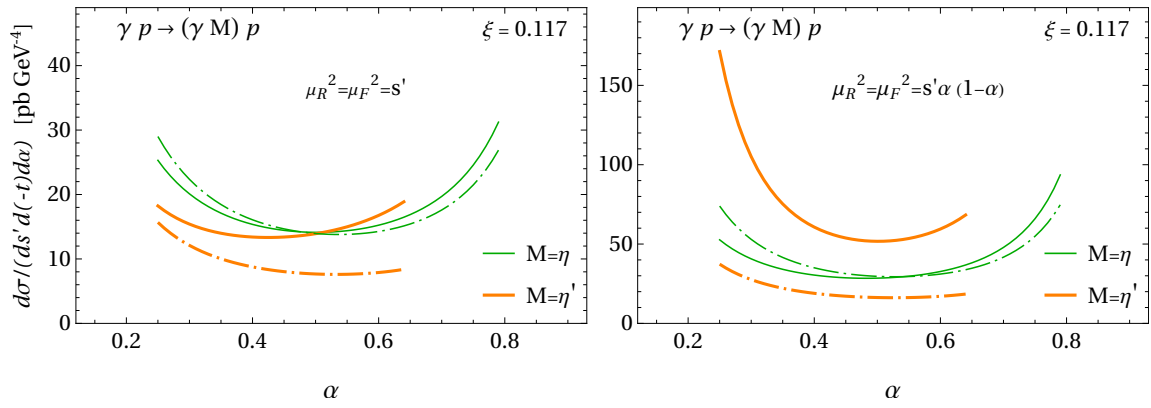


Figure 12: Fully differential cross-section for $\gamma p \rightarrow \gamma \eta(\eta') p'$, with η and η' shown by thin and thick lines, respectively. Dot-dashed lines represent quark-only contributions, while the solid lines also include the two-gluon contributions to η and η' . In the left figure the renormalization and factorization scales are set to $\mu_R^2 = \mu_F^2 = s'$, whereas in the right figure $\mu_R^2 = \mu_F^2 = s' \alpha (1 - \alpha)$. Both figures are evaluated at $s' = 4 \text{ GeV}^2$ and $S_{\gamma N} = 20 \text{ GeV}^2$, yielding $\xi = 0.117$, and at $(-t) = (-t_0)$.

E.2 Single differential cross-section

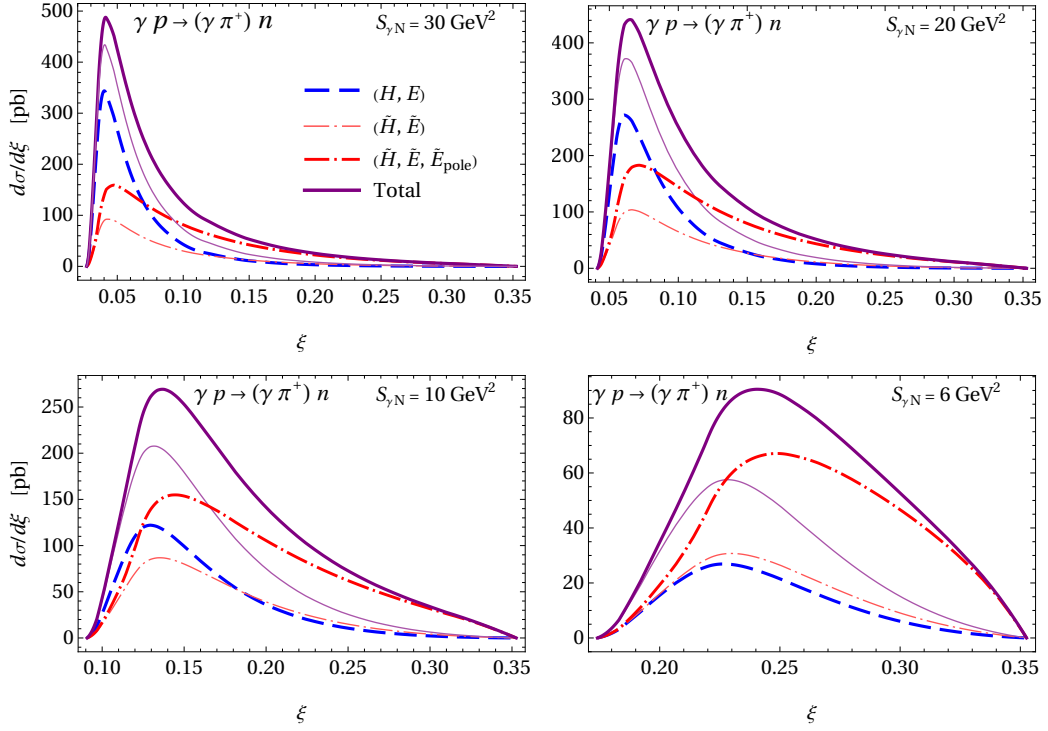


Figure 13: Single differential cross-section for $\gamma p \rightarrow (\gamma \pi^+) n$ at $S_{\gamma N} = 30, 20, 10,$ and 6 GeV^2 . Dashed and dash-dotted lines correspond to the vector and axial-vector GPD contributions, respectively, while solid lines show their sum, i.e., the total result. Thin lines denote axial and total results obtained without the π -pole contribution.

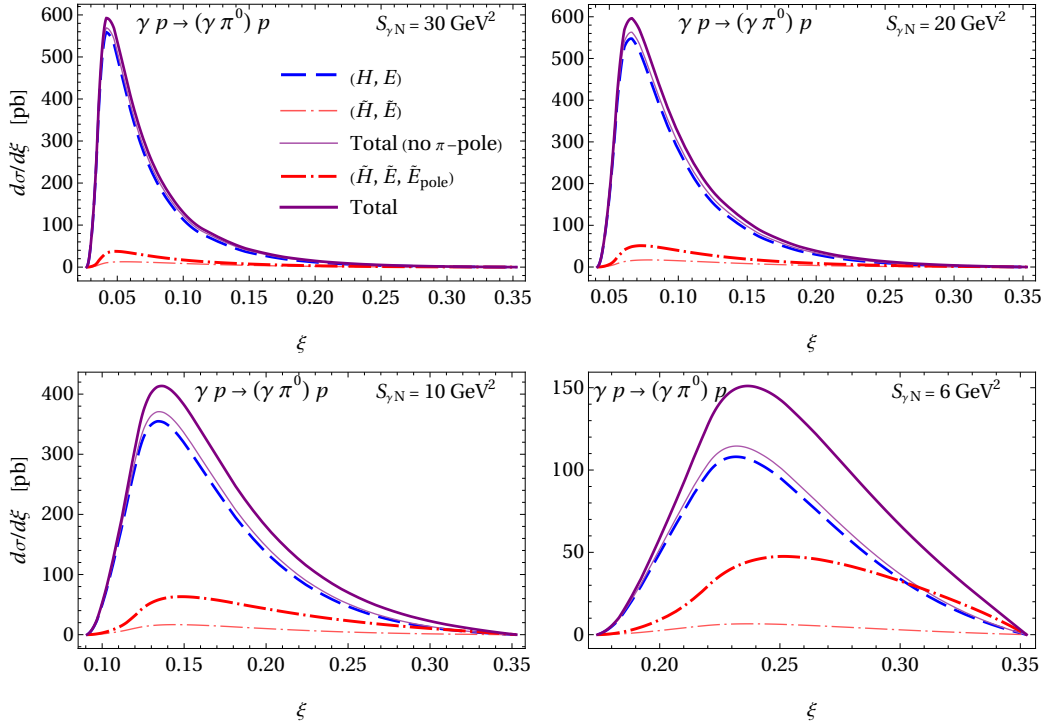


Figure 14: Single differential cross-section for $\gamma p \rightarrow (\gamma \pi^0) p$ at $S_{\gamma N} = 30, 20, 10,$ and 6 GeV^2 . Line designations as in Fig. 13.

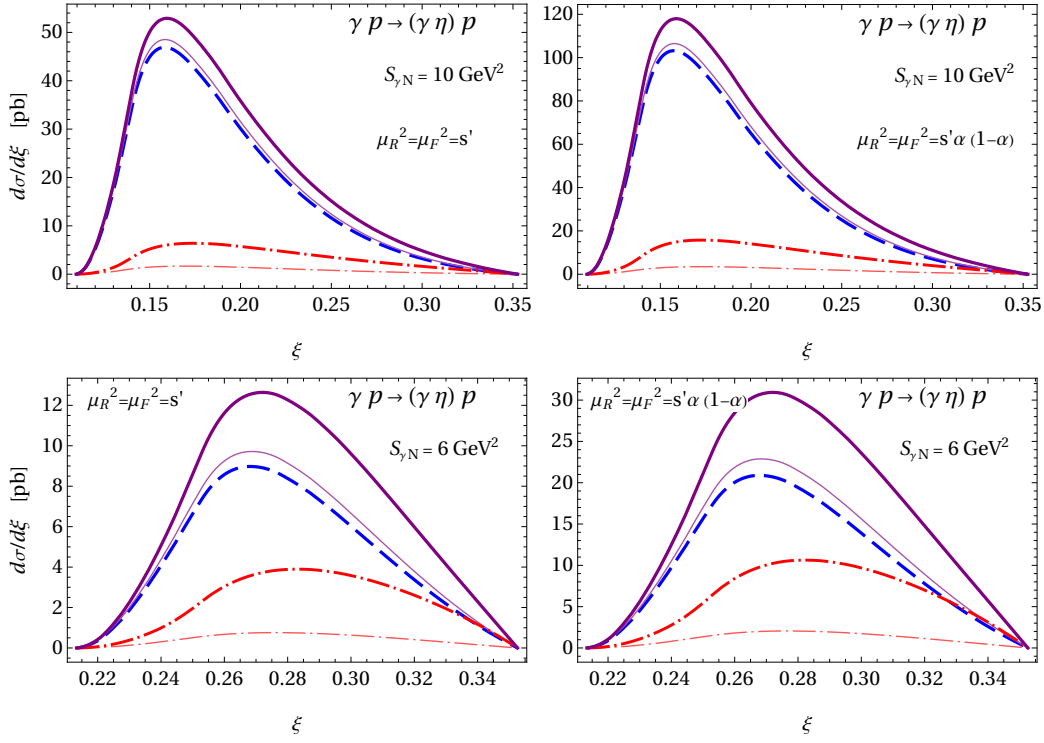


Figure 15: Single differential cross-section for $\gamma p \rightarrow (\gamma\eta)p$ at $S_{\gamma N} = 10$ and 6 GeV^2 , compared for the scale choices $\mu_R^2 = \mu_F^2 = s'$ and $\mu_R^2 = \mu_F^2 = s'\alpha(1-\alpha)$. Line designations as in Fig. 13.

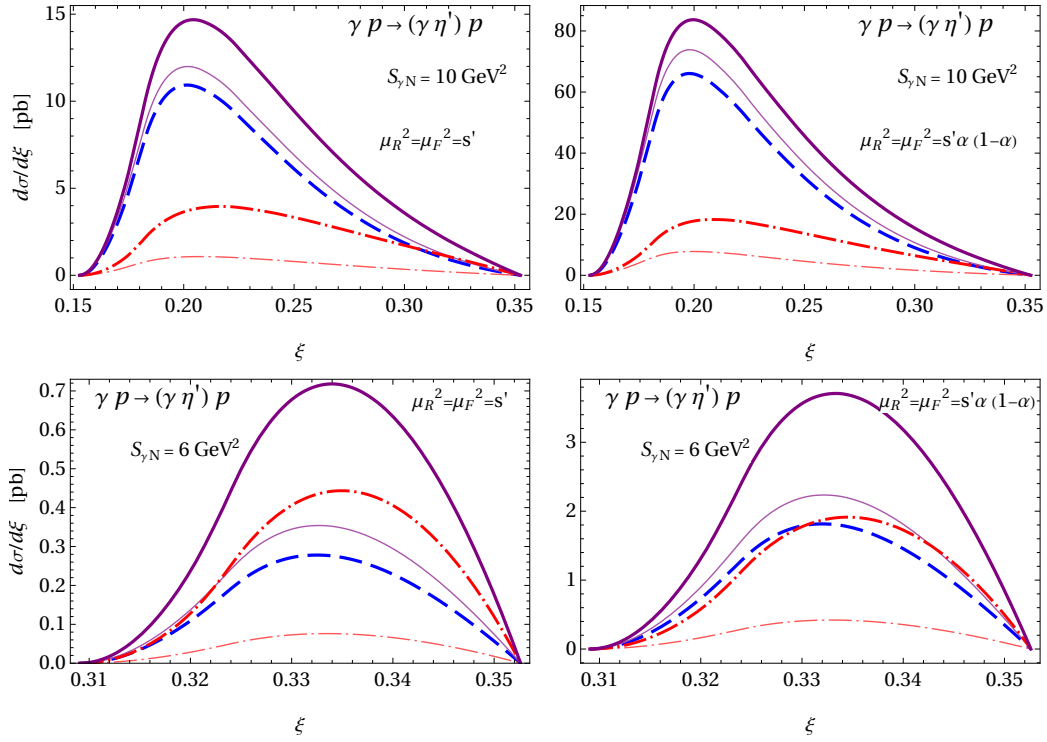


Figure 16: Single differential cross-section for $\gamma p \rightarrow (\gamma\eta')p$ at $S_{\gamma N} = 10$ and 6 GeV^2 , compared for the scale choices $\mu_R^2 = \mu_F^2 = s'$ and $\mu_R^2 = \mu_F^2 = s'\alpha(1-\alpha)$. Line designations as in Fig. 13.

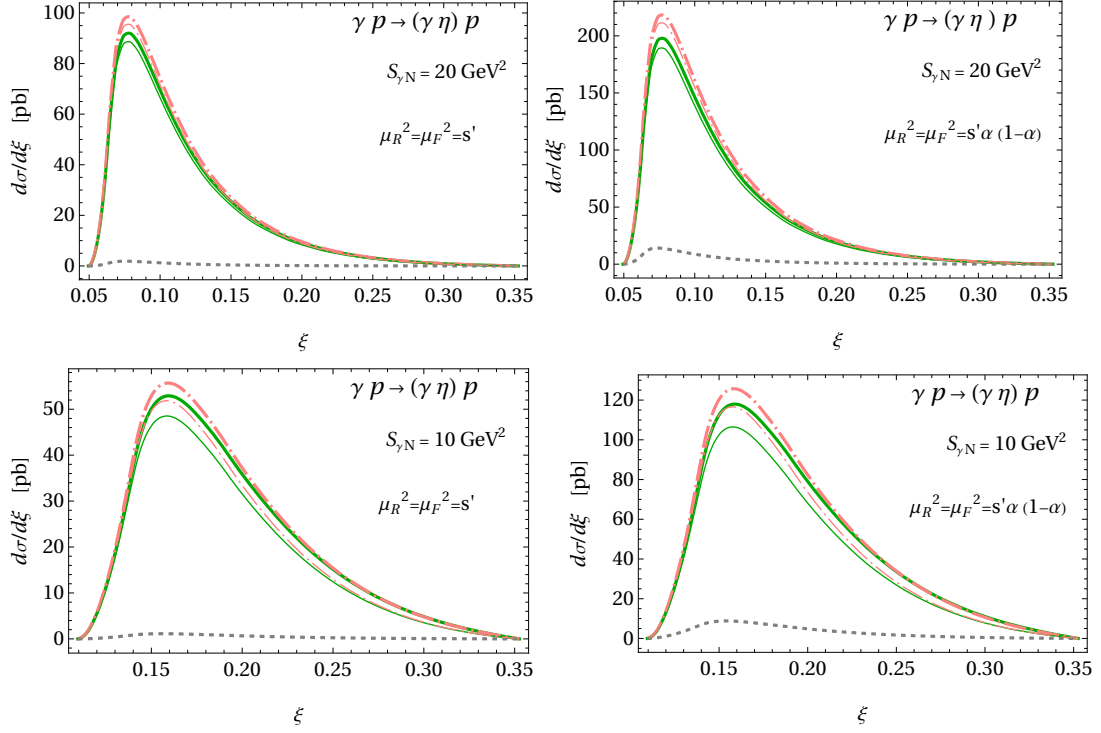


Figure 17: Single differential cross-section for $\gamma p \rightarrow (\gamma\eta)p$ at $S_{\gamma N} = 20$, and 10 GeV^2 , compared for the scale choices $\mu_R^2 = \mu_F^2 = s'$ and $\mu_R^2 = \mu_F^2 = s'\alpha(1-\alpha)$. Dot-dashed lines represent quark-only contributions, while the total contributions, denoted by solid lines also include the two-gluon contributions to η . For comparison, dotted lines correspond to gluon-only contributions. Thin lines represent results obtained without the π -pole contribution.

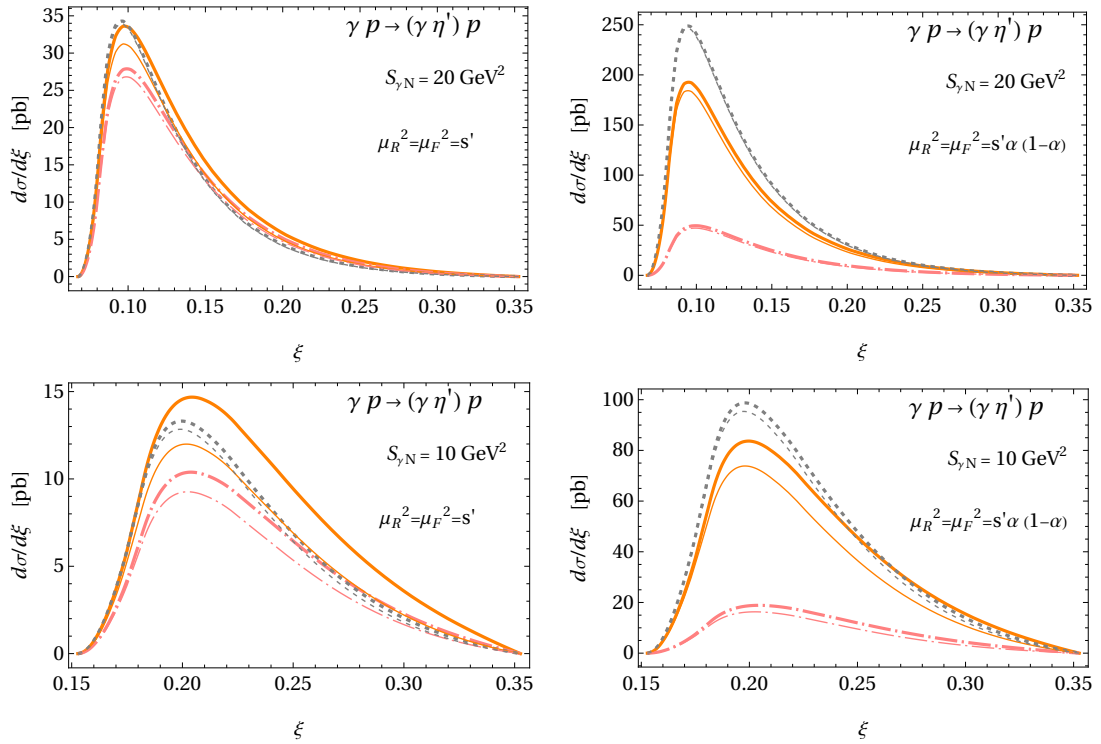


Figure 18: Single differential cross-section for $\gamma p \rightarrow (\gamma\eta')p$ at $S_{\gamma N} = 20$ and 10 GeV^2 , compared for the scale choices $\mu_R^2 = \mu_F^2 = s'$ and $\mu_R^2 = \mu_F^2 = s'\alpha(1-\alpha)$. Line designations as in Fig. 17.

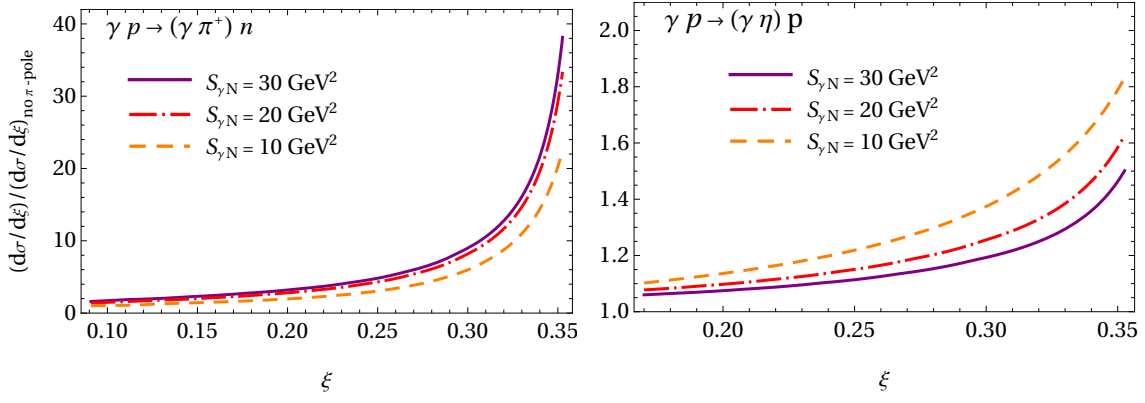


Figure 19: Ratio of the single differential cross-section (3.10) calculated with and without the π -pole contribution. Results at different kinematical settings are compared, specified by $S_{\gamma N} = 30, 20,$ and 10 GeV^2 . Left: $\gamma p \rightarrow \gamma \pi^+ n$. Right: $\gamma p \rightarrow \gamma \eta p$.

E.3 Integrated cross-section

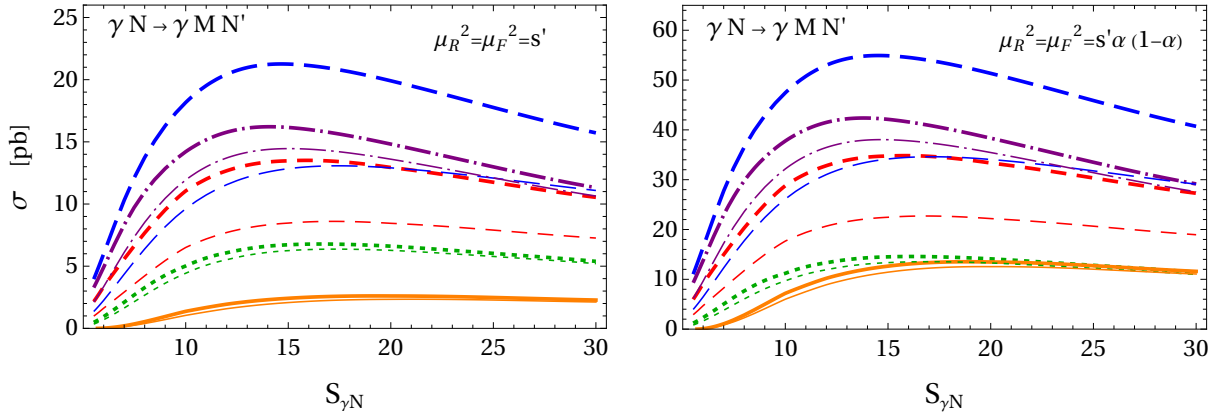


Figure 20: Cross-section for $\gamma N \rightarrow \gamma M N'$, with $M = \pi^+, \pi^-, \pi^0, \eta,$ and η' . Thick and thin lines denote results with and without the π -pole contribution, respectively. In the left figure the renormalization and factorization scales are set to $\mu_R^2 = \mu_F^2 = s'$, while in the right figure $\mu_R^2 = \mu_F^2 = s' \alpha (1 - \alpha)$. Line designations as in Fig. 21.

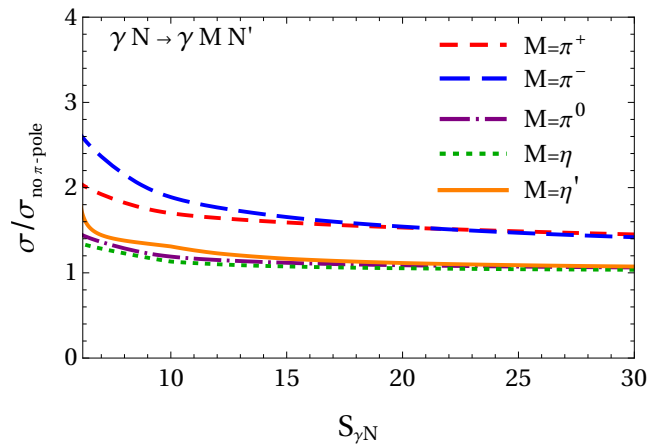


Figure 21: Ratio of the cross-sections (3.14) for $\gamma N \rightarrow \gamma M N'$, with $M = \pi^+, \pi^-, \pi^0, \eta,$ and η' , calculated with and without the π -pole contribution.

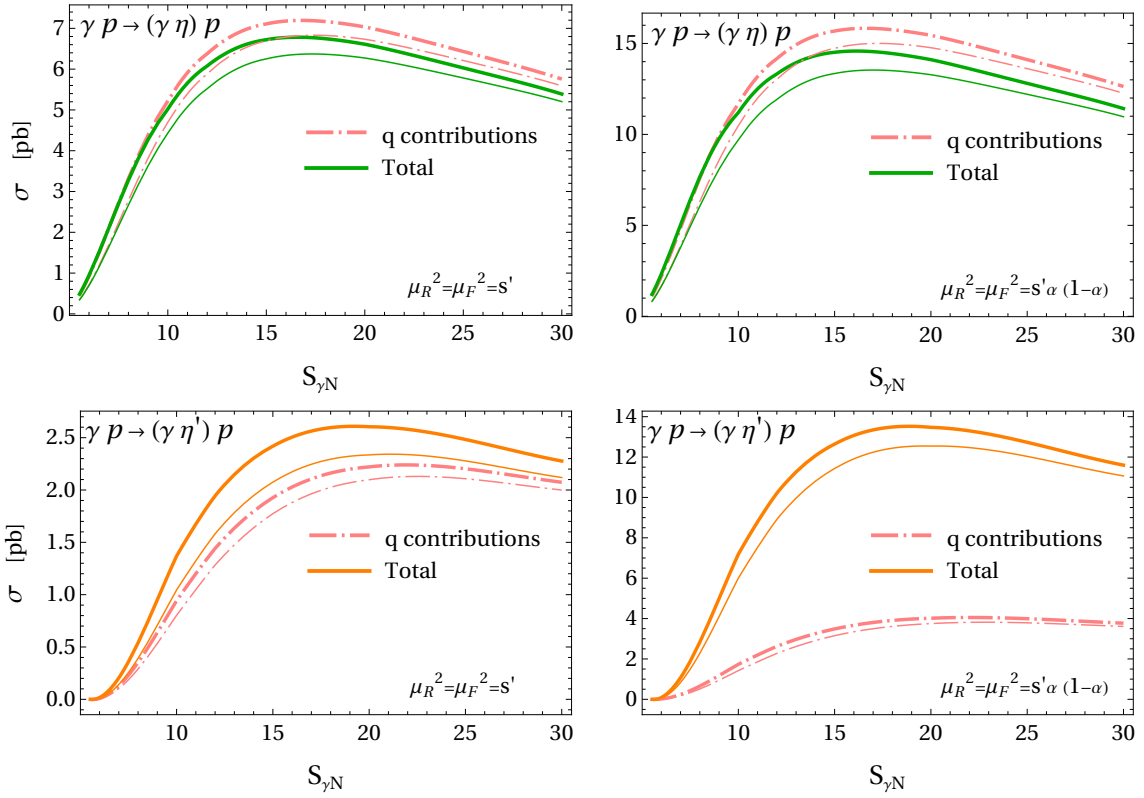


Figure 22: Cross-section for $\gamma p \rightarrow \gamma \eta(\eta') p$. Thick and thin lines denote results with and without the π -pole contribution, respectively. Dot-dashed lines represent quark-only contributions, while the total contributions, denoted by solid lines also include the two-gluon contributions to η and η' . In the left column the renormalization and factorization scales are set to $\mu_R^2 = \mu_F^2 = s'$, whereas in the right column $\mu_R^2 = \mu_F^2 = s' \alpha (1 - \alpha)$.

References

- [1] X.-D. Ji and J. Osborne, *One loop corrections and all order factorization in deeply virtual Compton scattering*, *Phys. Rev. D* **58** (1998) 094018 [[hep-ph/9801260](#)].
- [2] J. C. Collins and A. Freund, *Proof of factorization for deeply virtual Compton scattering in QCD*, *Phys. Rev. D* **59** (1999) 074009 [[hep-ph/9801262](#)].
- [3] J. C. Collins, L. Frankfurt and M. Strikman, *Factorization for hard exclusive electroproduction of mesons in QCD*, *Phys. Rev. D* **56** (1997) 2982–3006 [[hep-ph/9611433](#)].
- [4] N. d’Hose, S. Niccolai and A. Rostomyan, *Experimental overview of Deeply Virtual Compton Scattering*, *Eur. Phys. J.* **A52** (2016), no. 6 151.
- [5] K. Kumerički, S. Liuti and H. Moutarde, *GPD phenomenology and DVCS fitting*, *Eur. Phys. J.* **A52** (2016), no. 6 157 [[1602.02763](#)].
- [6] L. Favart, M. Guidal, T. Horn and P. Kroll, *Deeply Virtual Meson Production on the nucleon*, *Eur. Phys. J. A* **52** (2016), no. 6 158 [[1511.04535](#)].
- [7] M. Čuić, G. Duplančić, K. Kumerički and K. Passek-K., *NLO corrections to the deeply virtual meson production revisited: impact on the extraction of generalized parton distributions*, *JHEP* **12** (2023) 192 [[2310.13837](#)]. [Erratum: *JHEP* 02, 225 (2024)].
- [8] R. Boussarie, B. Pire, L. Szymanowski and S. Wallon, *Exclusive photoproduction of a $\gamma\rho$ pair with a large invariant mass*, *JHEP* **02** (2017) 054 [[1609.03830](#)]. [Erratum: *JHEP* 10, 029 (2018)].
- [9] G. Duplančić, K. Passek-Kumerički, B. Pire, L. Szymanowski and S. Wallon, *Probing axial quark generalized parton distributions through exclusive photoproduction of a $\gamma\pi^\pm$ pair with a large invariant mass*, *JHEP* **11** (2018) 179 [[1809.08104](#)].
- [10] J.-W. Qiu and Z. Yu, *Extraction of the Parton Momentum-Fraction Dependence of Generalized Parton Distributions from Exclusive Photoproduction*, *Phys. Rev. Lett.* **131** (2023), no. 16 161902 [[2305.15397](#)].
- [11] K. Deja, V. Martinez-Fernandez, B. Pire, P. Sznajder and J. Wagner, *Phenomenology of double deeply virtual Compton scattering in the era of new experiments*, *Phys. Rev. D* **107** (2023), no. 9 094035 [[2303.13668](#)].
- [12] D. Y. Ivanov, B. Pire, L. Szymanowski and O. V. Teryaev, *Probing chiral odd GPD’s in diffractive electroproduction of two vector mesons*, *Phys. Lett. B* **550** (2002) 65–76 [[hep-ph/0209300](#)].
- [13] R. Enberg, B. Pire and L. Szymanowski, *Transversity GPD in photo- and electroproduction of two vector mesons*, *Eur. Phys. J. C* **47** (2006) 87–94 [[hep-ph/0601138](#)].
- [14] M. El Beiyad, B. Pire, M. Segond, L. Szymanowski and S. Wallon, *Photoproduction of a $\pi\rho_T$ pair with a large invariant mass and transversity generalized parton distribution*, *Phys. Lett. B* **688** (2010) 154–167 [[1001.4491](#)].
- [15] M. Siddikov and I. Schmidt, *Exclusive production of quarkonia pairs in collinear factorization framework*, *Phys. Rev. D* **107** (2023), no. 3 034037 [[2212.14019](#)].

- [16] A. Pedrak, B. Pire, L. Szymanowski and J. Wagner, *Hard photoproduction of a diphoton with a large invariant mass*, *Phys. Rev. D* **96** (2017), no. 7 074008 [[1708.01043](#)]. [Erratum: *Phys.Rev.D* **100**, 039901 (2019)].
- [17] A. Pedrak, B. Pire, L. Szymanowski and J. Wagner, *Electroproduction of a large invariant mass photon pair*, *Phys. Rev. D* **101** (2020), no. 11 114027 [[2003.03263](#)].
- [18] O. Grocholski, B. Pire, P. Sznajder, L. Szymanowski and J. Wagner, *Collinear factorization of diphoton photoproduction at next to leading order*, *Phys. Rev. D* **104** (2021), no. 11 114006 [[2110.00048](#)].
- [19] O. Grocholski, B. Pire, P. Sznajder, L. Szymanowski and J. Wagner, *Phenomenology of diphoton photoproduction at next-to-leading order*, *Phys. Rev. D* **105** (2022), no. 9 094025 [[2204.00396](#)].
- [20] J.-W. Qiu and Z. Yu, *Exclusive production of a pair of high transverse momentum photons in pion-nucleon collisions for extracting generalized parton distributions*, *JHEP* **08** (2022) 103 [[2205.07846](#)].
- [21] J.-W. Qiu and Z. Yu, *Extracting transition generalized parton distributions from hard exclusive pion-nucleon scattering*, *Phys. Rev. D* **109** (2024), no. 7 074023 [[2401.13207](#)].
- [22] G. Duplančić, S. Nabeebaccus, K. Passek-Kumerički, B. Pire, L. Szymanowski and S. Wallon, *Accessing chiral-even quark generalised parton distributions in the exclusive photoproduction of a $\gamma\pi^\pm$ pair with large invariant mass in both fixed-target and collider experiments*, *JHEP* **03** (2023) 241 [[2212.00655](#)].
- [23] G. Duplančić, S. Nabeebaccus, K. Passek-Kumerički, B. Pire, L. Szymanowski and S. Wallon, *Probing chiral-even and chiral-odd leading twist quark generalized parton distributions through the exclusive photoproduction of a $\gamma\rho$ pair*, *Phys. Rev. D* **107** (2023), no. 9 094023 [[2302.12026](#)].
- [24] M. Siddikov, *Exclusive photoproduction of $\eta c\gamma$ pairs with large invariant mass*, *Phys. Rev. D* **110** (2024), no. 5 056043 [[2408.01822](#)].
- [25] J.-W. Qiu and Z. Yu, *Single diffractive hard exclusive processes for the study of generalized parton distributions*, *Phys. Rev. D* **107** (2023), no. 1 014007 [[2210.07995](#)].
- [26] S. Nabeebaccus, J. Schoenleber, L. Szymanowski and S. Wallon, *Breakdown of collinear factorization in the exclusive photoproduction of a $\pi^0\gamma$ pair with large invariant mass*, *Phys. Rev. D* **111** (2025), no. 3 034040 [[2311.09146](#)].
- [27] S. Nabeebaccus, J. Schoenleber, L. Szymanowski and S. Wallon, *Demonstration of collinear factorization breaking due to collinear-to-soft Glauber exchanges for a 23 exclusive process at leading twist*, *Phys. Rev. D* **111** (2025), no. 9 L091502 [[2409.16067](#)].
- [28] J. Botts and G. F. Sterman, *Hard Elastic Scattering in QCD: Leading Behavior*, *Nucl. Phys. B* **325** (1989) 62–100.
- [29] M. Fucilla, S. Nabeebaccus, L. Szymanowski, S. Wallon and J. Yarwick, *Exclusive photoproduction of a $\pi^0\gamma$ pair in the saturation framework*, **11**, 2025. [2511.11516](#).
- [30] S. V. Goloskokov and P. Kroll, *Vector meson electroproduction at small Bjorken- x and generalized parton distributions*, *Eur. Phys. J. C* **42** (2005) 281–301 [[hep-ph/0501242](#)].

- [31] S. V. Goloskokov and P. Kroll, *The Role of the quark and gluon GPDs in hard vector-meson electroproduction*, *Eur. Phys. J. C* **53** (2008) 367–384 [[0708.3569](#)].
- [32] S. V. Goloskokov and P. Kroll, *An Attempt to understand exclusive π^+ electroproduction*, *Eur. Phys. J. C* **65** (2010) 137–151 [[0906.0460](#)].
- [33] E. R. Berger, M. Diehl and B. Pire, *Time - like Compton scattering: Exclusive photoproduction of lepton pairs*, *Eur. Phys. J. C* **23** (2002) 675–689 [[hep-ph/0110062](#)].
- [34] V. N. Baier and A. G. Grozin, *Certain exclusive processes in QCD taking into account two-gluon states*, *Sov. J. Nucl. Phys.* **35** (1982) 596–605.
- [35] V. N. Baier and A. G. Grozin, *Hard hadron processes in QCD*, *Fiz. Elem. Chast. Atom. Yadra* **16** (1985) 5–58.
- [36] V. N. Baier and A. G. Grozin, *Gluonic contributions to the exclusive amplitudes*, *Z. Phys. C* **29** (1985) 161–165.
- [37] S. J. Brodsky and G. P. Lepage, *Large Angle Two Photon Exclusive Channels in Quantum Chromodynamics*, *Phys. Rev. D* **24** (1981) 1808.
- [38] B. Nižić, *Beyond leading order perturbative QCD corrections to $\gamma\gamma \rightarrow M^+ M^-$ ($M = \pi, K$)*, *Phys. Rev. D* **35** (1987) 80–101.
- [39] M. Benayoun and V. L. Chernyak, *$SU(3)$ Symmetry Breaking Effects in $\gamma\gamma \rightarrow$ Two Mesons Processes*, *Nucl. Phys. B* **329** (1990) 285–309.
- [40] P. Kroll and K. Passek-Kumerički, *The Two gluon components of the eta and eta-prime mesons to leading twist accuracy*, *Phys. Rev. D* **67** (2003) 054017 [[hep-ph/0210045](#)].
- [41] P. Kroll and K. Passek-Kumerički, *The η (η') gamma transition form factor and the gluon-gluon distribution amplitude*, *J. Phys. G* **40** (2013) 075005 [[1206.4870](#)].
- [42] P. Kroll and K. Passek-Kumerički, *On some implications of the BaBar data on the $\gamma^* \eta'$ transition form factor*, *Phys. Lett. B* **793** (2019) 195–199 [[1903.06650](#)].
- [43] P. Kroll and K. Passek-Kumerički, *Wide-angle photoproduction of the η' -meson and its gluon content*, *Phys. Rev. D* **105** (2022), no. 3 034005 [[2111.08965](#)].
- [44] **RQCD** Collaboration, G. S. Bali, V. M. Braun, S. Bürger, M. Göckeler, M. Gruber, F. Hutzler, P. Korcyl, A. Schäfer, A. Sternbeck and P. Wein, *Light-cone distribution amplitudes of pseudoscalar mesons from lattice QCD*, *JHEP* **08** (2019) 065 [[1903.08038](#)]. [Addendum: *JHEP* 11, 037 (2020)].
- [45] **Lattice Parton** Collaboration, J. Hua *et. al.*, *Pion and Kaon Distribution Amplitudes from Lattice QCD*, *Phys. Rev. Lett.* **129** (2022), no. 13 132001 [[2201.09173](#)].
- [46] X. Gao, A. D. Hanlon, N. Karthik, S. Mukherjee, P. Petreczky, P. Scior, S. Syritsyn and Y. Zhao, *Pion distribution amplitude at the physical point using the leading-twist expansion of the quasi-distribution-amplitude matrix element*, *Phys. Rev. D* **106** (2022), no. 7 074505 [[2206.04084](#)].
- [47] H.-n. Li, *Dispersive derivation of the pion distribution amplitude*, *Phys. Rev. D* **106** (2022), no. 3 034015 [[2205.06746](#)].

- [48] S. J. Brodsky and G. F. de Teramond, *Hadronic spectra and light-front wavefunctions in holographic QCD*, *Phys. Rev. Lett.* **96** (2006) 201601 [[hep-ph/0602252](#)].
- [49] T. Feldmann, P. Kroll and B. Stech, *Mixing and decay constants of pseudoscalar mesons*, *Phys. Rev. D* **58** (1998) 114006 [[hep-ph/9802409](#)].
- [50] M. Diehl, *Generalized parton distributions*, *Phys. Rept.* **388** (2003) 41–277 [[hep-ph/0307382](#)].
- [51] P. Kroll, H. Moutarde and F. Sabatie, *From hard exclusive meson electroproduction to deeply virtual Compton scattering*, *Eur. Phys. J. C* **73** (2013), no. 1 2278 [[1210.6975](#)].
- [52] I. V. Musatov and A. V. Radyushkin, *Evolution and models for skewed parton distributions*, *Phys. Rev. D* **61** (2000) 074027 [[hep-ph/9905376](#)].
- [53] A. V. Belitsky, D. Mueller and A. Kirchner, *Theory of deeply virtual Compton scattering on the nucleon*, *Nucl. Phys. B* **629** (2002) 323–392 [[hep-ph/0112108](#)].
- [54] L. Mankiewicz, G. Piller and A. Radyushkin, *Hard exclusive electroproduction of pions*, *Eur. Phys. J. C* **10** (1999) 307–312 [[hep-ph/9812467](#)].
- [55] M. Vanderhaeghen, P. A. M. Guichon and M. Guidal, *Deeply virtual electroproduction of photons and mesons on the nucleon: Leading order amplitudes and power corrections*, *Phys. Rev. D* **60** (1999) 094017 [[hep-ph/9905372](#)].
- [56] G. Duplančić and B. Nižić, *NLO perturbative QCD predictions for $\gamma\gamma \rightarrow M^+ M^-$ ($M = \pi, K$)*, *Phys. Rev. Lett.* **97** (2006) 142003 [[hep-ph/0607069](#)].
- [57] E. Maina and R. Torasso, *Pion Compton scattering in perturbative QCD*, *Phys. Lett. B* **320** (1994) 337–345 [[hep-ph/9309314](#)].
- [58] M. Tamazouzt, *Primakoff effect at high-energy*, *Phys. Lett. B* **211** (1988) 477–480.
- [59] C. Coriano and H.-N. Li, *The Transition to perturbative QCD in Compton scattering*, *Nucl. Phys. B* **434** (1995) 535–564 [[hep-ph/9405295](#)].
- [60] D.-F. Zeng and B.-Q. Ma, *Recalculation of pion Compton scattering in perturbative QCD*, *Phys. Lett. B* **542** (2002) 55–64 [[hep-ph/0202220](#)].
- [61] **Belle** Collaboration, S. Uehara *et. al.*, *High-statistics study of neutral-pion pair production in two-photon collisions*, *Phys. Rev. D* **79** (2009) 052009 [[0903.3697](#)].
- [62] **Belle** Collaboration, S. Uehara *et. al.*, *High-statistics study of eta pi0 production in two-photon collisions*, *Phys. Rev. D* **80** (2009) 032001 [[0906.1464](#)].
- [63] S. Arrigo, *Gamma+pi0 production in gluex*, in *Towards Improved Hadron Femtography with Hard Exclusive Reactions, Edition IV*, (Virginia Tech / Jefferson Lab, USA), 2025. Conference talk.
- [64] G. Duplančić, D. Müller and K. Passek-Kumerički, *Next-to-leading order corrections to deeply virtual production of pseudoscalar mesons*, *Phys. Lett. B* **771** (2017) 603–610 [[1612.01937](#)].